Stony Brook University

OFFICIAL COPY

Collimator Optimization for Single Photon Emission Computed Tomography

Using Detection and Localization Tasks

A Thesis Presented

by

Yihuan Lu

to

The Graduate School

in Partial Fulfillment of the Requirements

for the Degree of

Master of Science

in

Electrical Engineering

Stony Brook University

December 2011

Stony Brook University

The Graduate School

Yihuan Lu

We, the thesis committee for the above candidate for the

Master of Science degree, hereby recommend

acceptance of this thesis.

Gene Gindi, Thesis Advisor

Associate Professor, Department of Electrical & Computer Engineering

Petar Djuric, Second Reader

Professor, Department of Electrical & Computer Engineering

This thesis is accepted by the Graduate School

Lawrence Martin

Dean of the Graduate School

Abstract of the Thesis

Collimator Optimization for Single Photon Emission Computed Tomography

Using Detection and Localization Tasks

by

Yihuan Lu

Master of Science

in

Electrical Engineering

Stony Brook University

2011

We use signal detection and estimation and simulation methods to optimize the collimator in SPECT (Single Photon Emission Computed Tomography) medical imaging systems. A SPECT system images a radiopharmaceutical in the body to produce raw data called the sinogram that is then reconstructed to form a viewable image. The important imaging component is the collimator which controls a noise/resolution tradeoff in the sinogram. A signal like a tumor can be lost in the blur and noise of the sinogram. We apply an ideal observer to the sinogram to find the best collimator. We address two tasks (1) detect and localize a single signal; (2) detect and localize multiple signals. Task performance of the ideal observer is measured as area under the LROC (Location Receiver Operating Characteristic) curve for task (1), and area under the AFROC (Alternative free response ROC) curve for task (2). In general, we show that low efficiency collimators that yield blurry images with low relative noise outperform conventional clinical collimators that yield higher resolution but noisier images.

To my parents

Table of Contents

List of Figures

List of Tables

List of Abbreviations

AAFROC	Area Under AFROC curve
AFROC	Alternative Free Response ROC
ALROC	Area under the LROC curve
AROC	Area under the ROC curve
AUC	AROC
CL	Correct Localized
CT	Computed Tomography
FN	False Negative
FP	False Positive
FWHM	Full Width at Half of Maximum
GAP	General All Purpose
HR	High Resolution
IO	Ideal Observer
LROC	Location Receiver Operating Characteristic
MIPL	Medical Image Processing Laboratory
PET	Positron Emission Tomography
PSF	Point Spread Function
ROC	Receiver Operating Characteristic
SMF	Scanning Matched Filter
SPECT	Single Photon Emission Computed Tomography
SPT	Septal Thickness
TN	True Negative
TP	True Positive
UHR	Ultra High Resolution
UHsens	Ultra High sensitivity

Acknowledgments

Chapter 1

Introduction

1.1   Nuclear medicine

Nuclear Medicine is a branch or specialty of medicine and medical imaging that applies radioactive material to patients for the purpose of diagnosis and therapeutics. A doctor injects a radiopharmaceutical containing a both pharmaceutical and radionuclide into a patient's body. The radionuclide is an atom in the pharmaceutical that is radioactive and emits γ-rays in the 80-300 keV range. The pharmaceutical goes to an area of interest in the body by biological action. For example, the pharmaceutical may be designed to seek out tumors of a certain kind. It then emits γ-rays which are detected by detectors, and an estimate of γ-ray source density is made by a tomographic reconstruction. The reconstruction is a 3-D map of the spatial density of radionuclide. The physician views 2-D slices of the 3-D reconstruction. This form of nuclear medicine is known as emission tomography.

In recent decades, two emission tomographic techniques become widely used: single photon emission computer tomography (SPECT) and positron emission tomography (PET). In SPECT, radionuclide emits a single γ-ray in any direction and in one or more energies in the $80 - 300$ keV range. In PET, a positron emitter replaces the γ-emitter of SPECT. The positron is emitted, drifts a few mm, annihilates with an electron to emit two 511 keV γ-rays travelling 180° apart. This action of PET is exploited in the instrumentation to derive reconstructions. In this thesis we focus on SPECT.
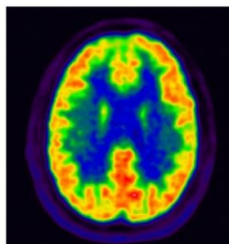
Figure 1.1 Transaxial brain image from PET
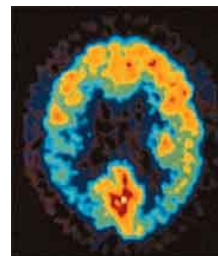
Figure 1.2 Transaxial brain image from SPECT

1.2   SPECT clinical applications

Applications in SPECT include cardiac imaging, where often the physician looks for a perfusion defect in the heart wall muscle. This shows up as a cold spot (a dip in radionuclide density). (Wernick & Aarsvold, 2004)Another application is in bone imaging(Parker & Anthony, 2011), where tomography shows up as bright spot of high radionuclide concentration. For a more comprehensive survey of applications, see (Wernick & Aarsvold, 2004).
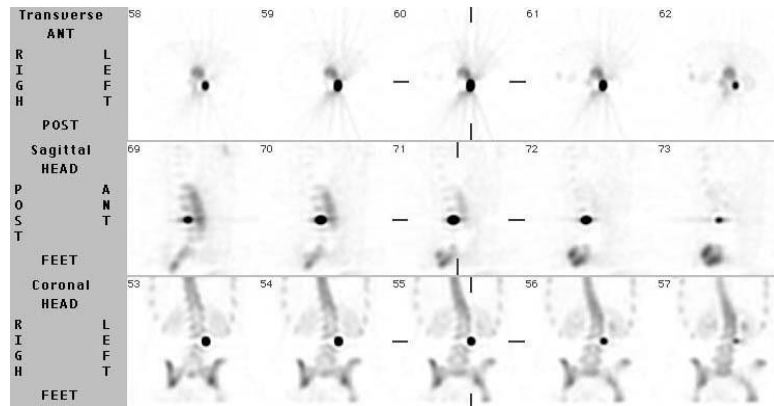
Figure 1.3 Bone image from SPECT(Parker & Anthony, 2011). The images show a tumor as a hot (dark) spot along the spine. The display is shown for slices at 3 orientations.
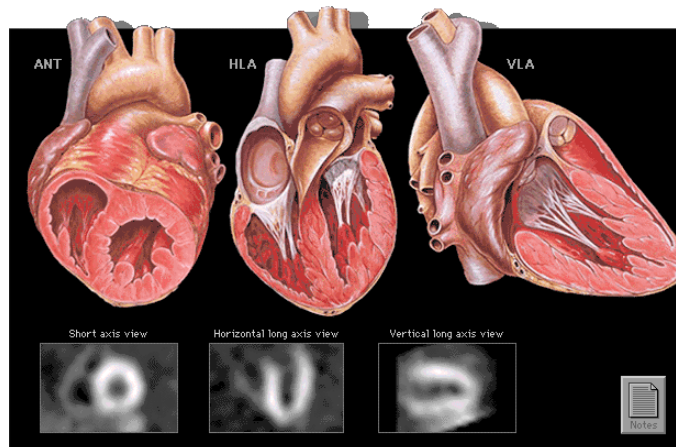
Figure 1.4 Heart image from SPECT. The anatomical drawings are along the top row and the corresponding SPECT image in the bottom row (Yale University School of Medicine, 2004)

Often the radionuclide used in studies above emits γ-rays at a single energy. For example, Tc99m which emits at 140 keV is used with an appropriate radiopharmaceutical for cardiac(Yale University School of Medicine, 2004) and bone imaging. In other applications, such as neuroendocrine tomography imaging (Lamberts, Chayvialle, & Krenning, 1992)**,** the radionuclide, in this case In-111, emits at two energies 172keV and 247 keV.

1.3   Emission tomography vs. computed tomography

Computed Tomography (CT) is a well-known imaging modality that is similar to SPECT in that the image is reconstructed from projection data (we will discuss reconstruction in more detail below). CT uses an external X-ray beam to irradiate the patient from many angles and SPECT uses the radiopharmaceutical to emit radiation from within the body. The SPECT radiation is collected from many angles. A reconstruction in CT is a map of the X-ray attenuation coefficient, whereas in SPECT it is a measure of radionuclide spatial density. A SPECT image looks considerably blurrier than the CT image and is of lower resolution. However, actually they tell different knowledge. For example, in the brain image Figure 1.5 and Figure 1.6, CT shows us more anatomical detail and SPECT gives us information about the metabolic activity in the brain. CT can provide high resolution anatomical information and SPECT can not only provide low-resolution anatomical structure, but also follow the absorption, distribution and metabolism of the radiopharmaceuticals and achieve the functional image of the organ of interest. (Khurd & Gindi, 2005)
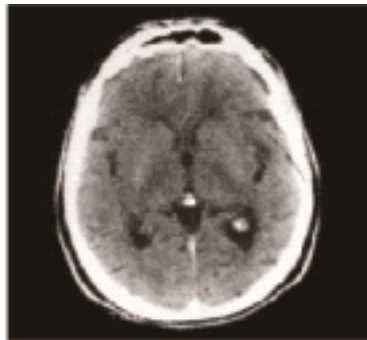
Figure 1.5 Transaxial brain image from CT
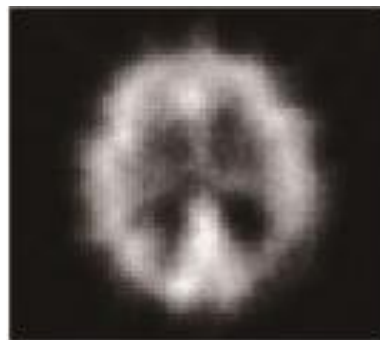
Figure 1.6 Transaxial brain image from SPECT

1.4   Planar emission imaging

Planar imaging is the foundation of 3D tomographic techniques. Thus, it's necessary to describe in it more detail. In planar imaging, the patient is positioned under a gamma camera. When the radioactive sources (injected by doctor) decay, they emit gamma rays and the detectors of the camera count the gamma photons which reflect the spatial distribution information of radiopharmaceuticals within the patient.

Assume that the only gamma rays counted are those with directions approximately perpendicular to the detector plane, as illustrated in Figure 1.7. This can be implemented by a collimator that allows photons in a certain angular range to pass. A collimator, which we'll discuss in much more detail, is essentially a metal plate with many parallel holes drilled in it. The plate blocks γ-rays, but the holes allow passage to the detector. The detection is a 2-D position sensitive detector. A description of detector technology can be found in(Wernick & Aarsvold, 2004).
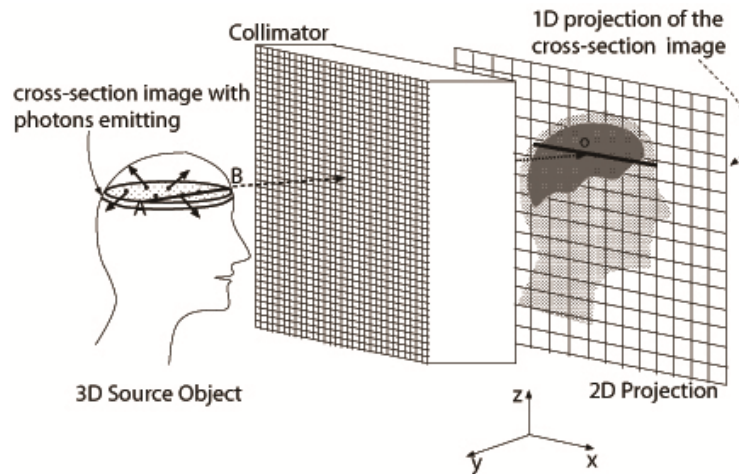
Figure 1.7 A 2D projection from a 3D object. See text for a detailed explanation

In Figure 1.7, we can see how planar imaging works. Any photon traveling along direction AB will hit the same spot "o" on the detector. As a consequence, all gamma rays emitted along strip AB in the patient contribute to the same detector location "o", and depth (distance to detector along y-axis) information is lost. Thus the measurement at "o" is approximately a line integral of the activity along the strip AB. Following this principle, the detected photons from a "slice" cross-section perpendicular to the detector plane (the figure shows one slice of the brain)

will form an image along one line, the one-dimensional projection. This is indicated by the dark line in Figure 1.7. A 2D projection is obtained from a 3D object by considering a stack of slices, as displayed in Figure 1.7 (Khurd, 2005). Note that the projection is formed at a particular angle about the Z-axis.

1.5   Emission imaging tomography aspects

For tomography, it needs projection views at many angles all around the object. By using a mathematical method to combine them, we can obtain the 3D structure. In SPECT, a gamma camera is designed to rotate up to 360 °around the patient. The camera stops at each equidistant sampling angle to collect gamma photons (projection data). As the projection data are acquired and stored, the computer will assimilate and process the data and do the reconstruction of the original radioactivity distribution of the human body.
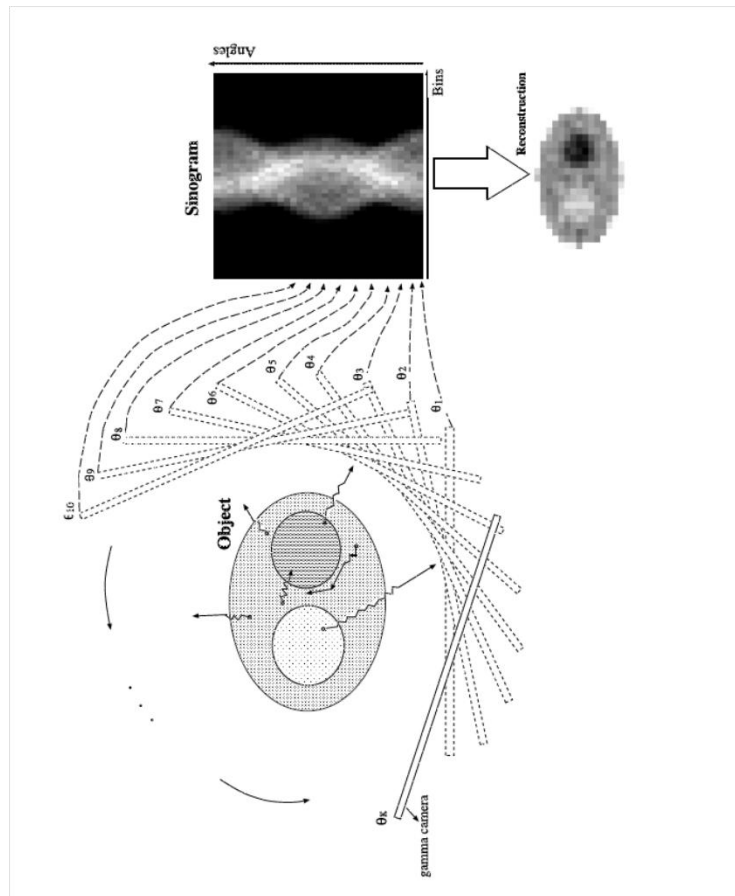
Figure 1.8 The basic principle of SPECT. (See text for explanation)

5

Figure 1.8 shows the basic principle of operation of a 2D SPECT system. The object can be treated as one slice of a 3D object, and the camera is a 1D camera. By rotating the camera, it obtains projection data at each angular position θ_k, k=1, 2, ...All of these projection data are then sequentially stacked to a 2D image with the abscissa being digitized detector coordinate "bin" and the ordinate being index of sample angles. This 2D digital image is referred as the "sinogram"(Khurd, 2005). It is called a sinogram because a single point in the object space causes a sine wave in the sinogram.

A typical "sinogram" is shown in Figure 1.8. We can easily see that the sinogram itself is not interpretable. Thus, in order to serve a diagnostic purpose, another important step needs to be done, which is called reconstruction. A reconstruction algorithm attempts to transform a sinogram to a meaningful image of the original coordinate frame. Typically, after feeding the sinogram to a computer system, the reconstruction algorithm will be executed there. The reconstruction images are usually for diagnostic or therapeutic purposes. The lower right image in Figure 1.8 shows a reconstruction of the object. In this thesis, we will not talk about reconstruction in detail since we are focusing on the image acquisition process, which ends up with a sinogram.

1.6　　Image quality in SPECT

Engineers seek to improve imaging systems. One way to measure improvement is by task performance. For example, if tumor detection is deemed a significant task and an appropriate measure of performance can be defined, and then system A is considered better than system B if A has better task performance.

What aspects of a SPECT system can we change to get better performance? We might alter the reconstruction algorithm. Or, we could alter the imaging system itself. In our work, we consider the problem of optimizing the collimator, which is the key component of a SPECT imaging and controls a noise-resolution tradeoff in the sinogram. We describe collimators in detail later.

1.7   Outline of thesis

Our basic goal is to study collimator optimization in the context of task performance.

In Chapter 2, we mathematically describe the formation of the sinogram and the character of the noise in the sinogram. In Chapter 3, we review the tasks we will consider. One task, called the LROC task, is the clinically important task of jointly detecting and localizing a single signal. (Here a "signal" could be a tumor.) Another task is the even more clinically realistic detection and localization of multiple signals. This is termed the AFROC task. These tasks are performed by ideal observers, which maximize performance.

In Chapter 4, we consider a planar SPECT system and assess the performance of the LROC task as the collimator properties are varied, thus yielding an optimal collimator. We compare this performance to a sub-optimal observer and show the differences in performance behavior. In Chapter 5, we analyze LROC performance as a function of collimator properties. In Chapter 6, we analyze AFROC performance of collimators for a case of detecting and localizing *two* signals (instead of one).

Chapter 7 is a summary and suggestions for future work. Chapter 7 also summarizes the contributions of the thesis.

Chapter 2

Imaging Model

As mentioned in chapter 1, a SPECT medical imaging system has several steps involved before obtaining the final reconstruction images. However, in this thesis, we only focus on sinogram which is the projection data. In this chapter, we will describe mathematically the formation of the sinogram. This is the "forward model" needed for later work.

2.1   Notational conventions

For expressive convenience, much of the notation used in this thesis will be explained here. We use plain italic lower-case letters to denote scalar variables and scalar-valued functions. Upper-case letters are used to denote scalar constants. Lower-case bold letters represent vectors or vector-valued functions. Their elements are specified by corresponding low-case (italic, not bold) quantities with an appropriate subscript. For instance, x_m, m=1, 2, …, N are all elements of N-dimensional vector $\mathbf{x}$. Bold upper-case letters denote matrices, such as the matrix $\mathbf{B}$. We use the subscripts of appropriate indices to indicate the elements of a matrix, such as $\mathbf{B}_{mn}$, which is the element of $\mathbf{B}$ located at row m and column n. A matrix-vector product would be $\mathbf{Bx}$ and we use the notation $\left[\mathbf{Bx}\right]_m$ to indicate its mth component. $\mathbf{XY}$ means the conventional matrix-matrix product. And $[\mathbf{XY}]_{mn}$ is element of the product result located at row m and column n. Another operation is $*$, which represents discrete convolution. The transpose notation of matrix $\mathbf{B}$ is $\mathbf{B^T}$.

As the need of statistical feature description for random quantities, we use the concepts of means and variances frequently in this project. Following the statistical conventions, we denote means by the decoration of a bar, such as $\bar{a}$ is the mean of a random variable a. The probability density function (pdf) is $p(a)$. Similarly $\bar{\mathbf{x}}$ and $p(\mathbf{x})$ are the mean and pdf of random vector $\mathbf{x}$. Another decoration used is the carat (^). The estimate of an unknown $\mathbf{f}$ is denoted $\hat{\mathbf{f}}$.

2.2   Definition of the object

8

Although in the real world the object should be described by continuous functions, we here only talk about our object, $\mathbf{f}$ as a discretized one. The continuous object is discretized into N pixels. These pixels are row-by-row lexicographically ordered by index n=1,2,…,N. If the object is 3D, we need x, y and z, three coordinates to localize one voxel f_n. In this case, our lexicographic order should be row-by-row first (one slice described by x and y), then slice number (z). Figure 2.1 and Figure 2.2 illustrate.

Actually, f_n is a measure of radionuclide density. We measure f_n by the mean number of photons emitted into all space per unit time. This number is Poisson distributed (Barrett & Myers, 2003). Then f_n is the mean number counts emitted from voxel n into all space per unit time.
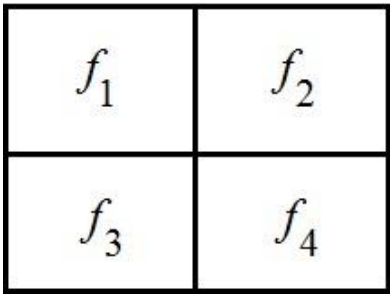
Figure 2.1 2D object pixel index
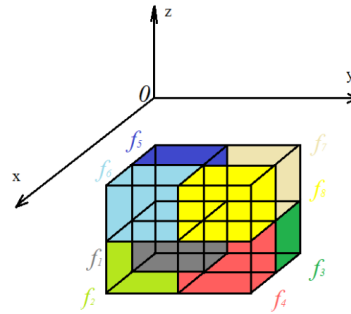
Figure 2.2 3D object voxel index

2.3   Definition of sinogram
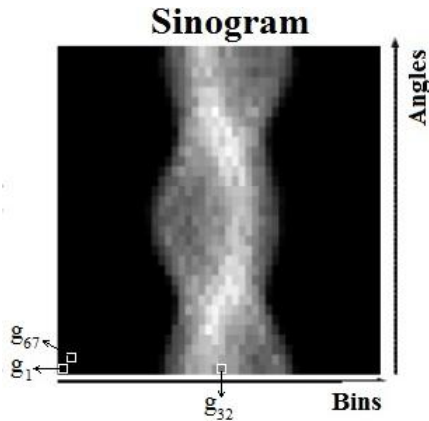
Figure 2.3 2D Sinogram

9

For the projection data, we use a discretized sinogram $\mathbf{g}$ to describe it. We also use lexicographic ordering to index g_m, m=1, 2, …, M. The quantity g_m is the number of counts received into the mth pixel of the camera. We call such a pixel a "detector bin", or simply a "bin". Vector $\mathbf{g}$ will be integer valued ($g_m \geq 0$) and is random. As shown in Figure 2.3, for each camera angle, we collect photons in 65 bins. Our lexicographic ordering is a bin-by-bin scheme, where each row is the bins at one angle and there is one row per angle.

2.4   System matrix $\mathbf{H}$

The imaging system is linear and summarized by a system matrix $\mathbf{H}$. Matrix element $\mathbf{H}_{mn}$ is proportional to the probability that a photon emitted from n is detected at bin m. We know that the number of photons emitted from n is Poisson with mean f_n. Each photon is then selected by a Bernoulli process of probability $\mathbf{H}_{mn}$ to be detected at bin m. It can be shown(Wang, 1997), that g_m is also Poisson and that its mean $\bar{g}_m$ is $\bar{g}_m = \sum_n \mathbf{H}_{mn} f_n$, or in more compact notation

$$\bar{\mathbf{g}} = \mathbf{Hf} \tag{2.1}$$

Furthermore, it can be shown that the counts in $\mathbf{g}$ are independent(Wang, 1997). Putting these facts together we can immediately write

$$p(\mathbf{g}\,|\,\mathbf{f}) = \prod_{m=1}^{M} \frac{e^{-[\mathbf{Hf}]_m}}{g_m!} ([\mathbf{Hf}]_m)^{g_m} \tag{2.2}$$

This is interpreted as a likelihood for $\mathbf{f}$ since $\mathbf{g}$ is observed.

In SPECT, this Poisson model is important since bin counts are typically fairly low, with a good percentage of the bins containing < 10 counts. The reason for such low counts is that very few photons pass through the collimator holes, about 1 in 10^4.

The system matrix models several different physical effects that control the propagation of a photon from $n \rightarrow m$. Importantly it summarizes the collimator. The collimator serves to accept only those photons that arrive approximately perpendicularly to the camera face.

2.5   Collimator

For simplicity, assume the collimator is made of a material like lead that completely blocks photons (Most collimators are in fact lead). Let's say the collimator was formed by drilling very small diameter very long holes in the lead, and assume these holes were closely spaced. In that case, only those source points along a line perpendicular to the collimator can be detected, so the collimator measures line integrals of **f**, as shown in Figure 2.4.
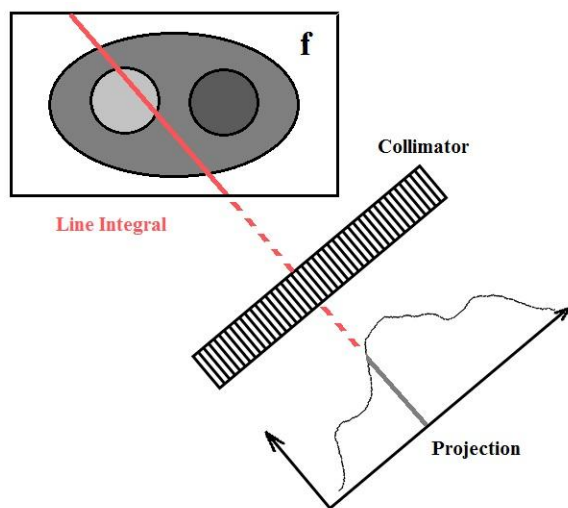
Figure 2.4 An infinitely fine collimator measures line integrals of f. The plot shows the 1-D projection of the 2-D object seen by the detector. The object is integrated along the red line.
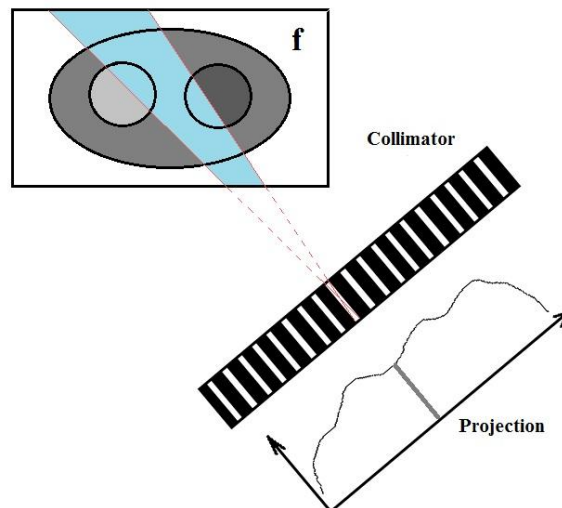
Figure 2.5 A more realistic collimator has finite width and finite length holes, and integrates the object along a conical region as shown.

In practice, the collimator is a lattice of finite sized holes of finite length. In this case, the collimator accepts rays from a finite cone angle as seen in Figure 2.5.

11
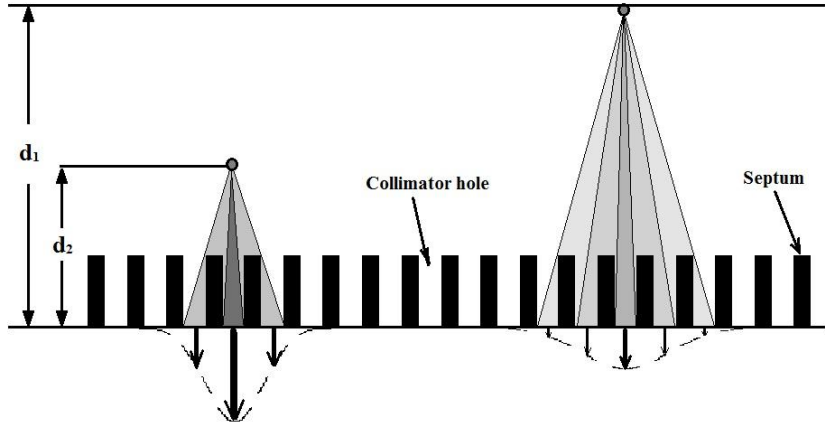
Figure 2.6 Prints at different depth yield different point-spread functions on the detector space. The solid angle between septa as seen by the point is proportional to the number of counts received between those septa.

The integration along the conical region is not equally weighted. Points closer to the collimator see a larger solid angle and $\mathbf{H}_{mn}$ is larger for these points. To describe this more quantitatively define depth d as the distance from an object point to the detector plane (The detector plane is right behind the collimator). Consider 2 points at different depths, d_1 and d_2, as seen in Figure 2.6. The farther point yields a blob, a point spread function that is wide and of low intensity, and the nearby point a thinner blob of higher intensity. For the parallel-hole collimators of interest to us, the blobs are approximately Gaussian (Wernick & Aarsvold, 2004) when averaged laterally across position. Figure 2.7 shows a piece of a real parallel hexagonal collimator. Figure 2.8 displays the Gaussians as a function of depth.
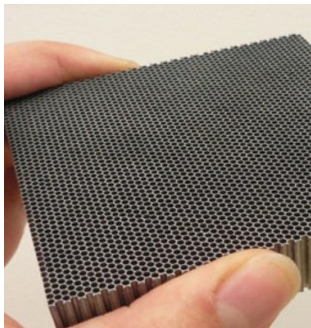
Figure 2.7 Partial real parallel collimator (Clinical collimator size is around 40 by 30 cm).
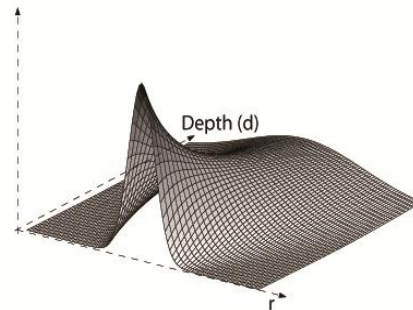
Figure 2.8 Depth-dependent collimator blur kernels.

12

One can characterize for a given collimator the depth-dependent width by (Zhou & Gindi, 2009)

$$FWHM(d) = \sqrt{\left(\frac{D}{l}d\right)^2 + (2.35\sigma_0)^2} , \qquad (2.3)$$

where FWHM is the Full Width at Half Max of the psf, and d is the distance from source to the crystal face. D is the bore diameter (definition of D will be shown later), l is the bore length and σ_0 is intrinsic camera resolution. The intrinsic camera resolution σ_0 is the standard deviation of the psf due to camera blur alone, i.e. that part of the blur that is collimator independent. Equation (2.3) tells you the width of the point spread function (PSF) but not its "height". Its height can be measured by average efficiency, which is defined as the fraction of emitted photons that pass through the collimator and reach the camera plane (Wernick & Aarsvold, 2004). Here, our efficiency is averaged over source position. It depends on the fine structure of the collimator.
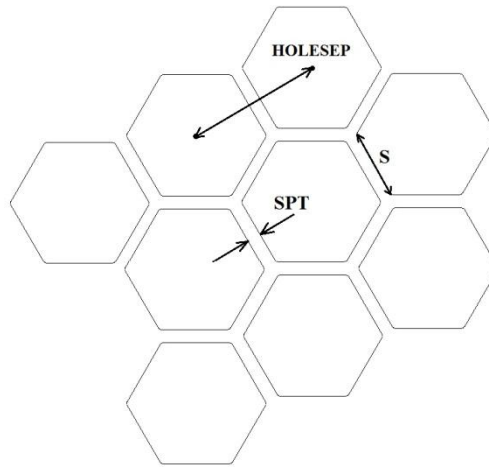
Figure 2.9 Hexagonal collimator, see text for details

As an example, consider a collimator made of hexagonal holes placed on a hexagonal array as shown in Figure 2.9. (A real version is shown in Figure 2.7) The collimator efficiency is determined by bore diameter D, bore length l and septal thickness (SPT). The septal thickness is the thickness of the lead separating the holes. From(Wernick & Aarsvold, 2004), the bore diameter D is defined by the relation (area of the hole) $= \frac{\pi}{4}D^2$. Here we use a hexagonal bore shape, and thus $D=1.819S$, where S is the length of one of the hexagonal sides, as shown in Figure 2.9. HOLSEP is defined as the distance between the centers of adjacent bores in the

13

lattice. Here, we have (Wernick & Aarsvold, 2004) $\text{SPT} = \text{HOLSEP} - \dfrac{\sqrt{\pi}}{\sqrt[4]{12}} D$. With all these

definitions, the average (over point source position) collimator efficiency for a hexagonal lattice is given by:

$$Average \quad efficiency = \frac{2}{\sqrt{3}} \frac{\pi D^4}{64 l^2 \left[\dfrac{\sqrt{\pi}}{\sqrt[4]{12}} D + SPT \right]^2}. \tag{2.4}$$

Interestingly, the efficiency of a point source is approximately independent of its position (lateral position and depth). So the average (over point position) efficiency is approximately the same as the efficiency of a single point. A typical value of average efficiency is about 2×10^{-4}. With (2.3) and (2.4) together, we can characterize the collimator. Thus (2.3) is a measure of resolution and (2.4) a measure of noise behavior. (A more efficient collimator collects more photons and so has less relative noise)

The depth-dependent behavior and efficiency are easily encoded into the system matrix $\mathbf{H}$. The matrix $\mathbf{H}$ is large but can be stored in RAM and used to compute projections $\mathbf{Hf}$.

So far, we have considered an object as if it were in air. But the radiopharmaceutical sits in the body. When a photon is emitted, it can interact with the atoms in the body in two ways: (1) it can be absorbed(Barrett & Swindell, 1981). (2). It can scatter into a new direction and perhaps still be detected. Both these attenuation and scatter effects are important areas of study. These effects can also be modeled in $\mathbf{H}$ (Xing, 2003). However, this topic is beyond the scope of this thesis and we will consider $\mathbf{H}$ to model only collimator effects.

The main goal of the thesis is to optimize the imaging system, and the collimator is the crucial element. Note that an efficient collimator has poor resolution and a high resolution collimator has poor efficiency. This resolution-noise tradeoff is at the heart of this thesis since it controls image quality.

So far we have talked about image formation, which we can rewrite here as

$$\mathbf{g} = \mathbf{Hf} + \mathbf{n} \tag{2.5}$$

where the Poisson noise $\mathbf{n}$ is written as if it were additive, but this does not lose generality. In

SPECT, the data $\mathbf{g}$ are reconstructed into a viewable image $\hat{\mathbf{f}}$ via some reconstruction algorithm, for example, the well known Filtered Backprojection algorithm(Wernick & Aarsvold, 2004).

As we will see later, we are interested in obtaining the best possible task-dependent image quality in the raw data $\mathbf{g}$, not in $\hat{\mathbf{f}}$. To do this we will make use of novel tasks and ideal observers (we will define ideal observer in the next chapter). In(Barrett & Myers, 2003), the case is made that tomographic imaging systems (in our case, the imaging system is the collimator and its placement relative to the object) should be designed so that an ideal observer inspecting the sinogram yields maximal task performance. The subsequent reconstruction algorithm should then be designed so that a *human* observer yields maximal task performance. In this thesis, we focus only on the first half of the problem – the design of the imaging system. One reason for this strategy is that often, the imaging hardware is designed without reference to a particular reconstruction algorithm, or the reconstruction algorithm might be changed many times during the lifetime of the imaging system. In this case, the collimator designed with an ideal observer yields the sinogram with the maximum information.

Chapter 3

Tasks and Observers

3.1 Introduction

We will optimize collimators by measuring the performance of a mathematical observer that observers the sinogram $\mathbf{g}$. There is evidence (Zhou, Kulkarni, Liu, & Gindi, 2009) that a collimator optimized this way will lead to a sinogram that gives good image quality in the reconstruction. Here we stick to the collimator optimization, and do not address the problem of optimizing the reconstruction.

We will summarize the receiver operating characteristic (ROC), localization ROC (LROC) and alternative free-response ROC (AFROC) curves and associated ideal observers and tasks. In our lab, we pioneered the formulation of ideal observers for the LROC (Khurd & Gindi, 2005) and AFROC (Khurd, Liu, & Gindi, 2010) tasks. These were abstract formulations. The goal here is to apply these to SPECT.

3.2 ROC

We first describe the ROC curve to establish concepts and definitions though we do not use it in our experiments. The ROC curve is used in analyzing 2-class detection tasks. In medical imaging, this task is "Is a signal (tumor) present or absent?" Here, the signal is added to a known background and the location of the signal is considered known and the form of the signal known exactly. Let the signal-present object be $\mathbf{f}_+ = \mathbf{s} + \mathbf{b}$, where $\mathbf{b}$ and $\mathbf{s}$ are the known background and signal. Then the signal-absent object is $\mathbf{f}_- = \mathbf{b}$. Let H_1 denote the hypothesis "signal present" and H_0 "signal absent". We use $\mathbf{f}$ to stand for either $\mathbf{f}_+$ or $\mathbf{f}_-$.

The image is $\mathbf{g}$, which will be $\mathbf{g}_+ = \mathbf{H}(\mathbf{f}_+) + \mathbf{n} = \mathbf{H}(\mathbf{b} + \mathbf{s}) + \mathbf{n}$ or $\mathbf{g}_- = \mathbf{H}(\mathbf{f}_-) + \mathbf{n} = \mathbf{H}\mathbf{b} + \mathbf{n}$ with $\mathbf{n}$ the Poisson noise. An *observer T* examines $\mathbf{g}$ and reports a scalar observer response $T(\mathbf{g})$.

In the standard method of 2-class decision strategy, we compare $T(\mathbf{g})$ to a scalar decision threshold T_0 :

$$
\begin{aligned}
Decide \quad & H_1 \quad && if \quad T(\mathbf{g}) \geq T_0 \\
& H_0 \quad && if \quad T(\mathbf{g}) < T_0
\end{aligned}
\tag{3.1}
$$

The threshold depends on many things. For example, a doctor may want to decide "tumor-present", even if $T(\mathbf{g})$ is low, just to be safe. Because it is difficult to specify a unique T_0 , the scalar figure of merit for performance should not depend on a specific T_0 .

One can make a true positive (TP) decision by choosing H_1 for $\mathbf{g}_+$, a false positive (FP) by choosing H_1 for $\mathbf{g}_-$, a false negative (FN) by choosing H_0 for $\mathbf{g}_+$ and a true negative (TN) by choosing H_0 for $\mathbf{g}_-$. It is customary to use $TP\ FP\ FN\ TN$ to stand for the probability of making such decisions. So sometimes the terms "TP rate" or "FP rate" are used. Since $FP + FN = 1.0$ and $TP + FP = 1.0$, one can summarize performance by using TP and FP only.

As T_0 varies, the TP and FP rates vary. A plot of TP vs FP as T_0 varies as seen in Figure 3.1 is the ROC curve. Clearly curve A is better than curve B because at any FP rate, curve A delivers a better TP rate.
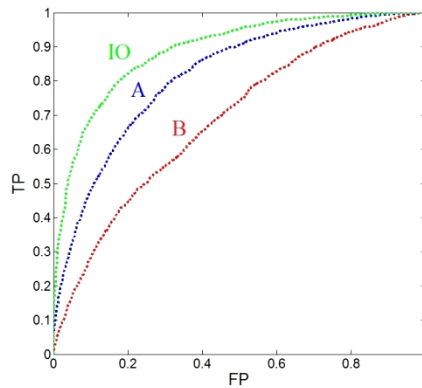
Figure 3.1 ROC Curves. The curve "IO" from the ideal observer lies above all possible ROC curves from other observers.

The ROC curve depends on the form of the observer $T(\mathbf{g})$. An ideal observer (IO) is one which gives the *best* ROC curve. In this case, the best curve is the one that lies above all other ROC curves from other observers. This is shown in Figure 3.1.

It is easy to see that a good figure of merit for an ROC curve is the area under the ROC curve, denoted AROC. The IO maximizes AROC (or AUC). Indeed, one strategy to compute the IO is to use this maximal area strategy (Barrett & Myers, 2003) via the Neyman Pearson lemma. The resulting IO curve has max AROC for any sub range of FP. The well known form of the IO for the ROC task is

$$T(\mathbf{g}) = \frac{p(\mathbf{g}\,|\,H_1)}{p(\mathbf{g}\,|\,H_0)} \equiv LR(\mathbf{g}) \tag{3.2}$$

where $p(\mathbf{g}\,|\,H_1)$, $p(\mathbf{g}\,|\,H_0)$ are the likelihoods of $\mathbf{g}$ under hypotheses H_1 and H_0, respectively. We denote this ratio as $LR(\mathbf{g})$. i.e. the "likelihood ratio" for given sinogram $\mathbf{g}$.

We can use (2.2) to compute $LR(\mathbf{g})$ for the ROC case. For H_1 we take $\mathbf{f} = \mathbf{f}_+$ and for H_0 take $\mathbf{f} = \mathbf{f}_-$, then $\overline{\mathbf{g}} = \mathbf{H}(\mathbf{b}+\mathbf{s})$ for the H_1 hypothesis. Substituting into (2.2) we get

$$p(\mathbf{g}\,|\,H_1) = \prod_m \frac{e^{-\mathbf{H}(\mathbf{b}+\mathbf{s})}[\mathbf{H}(\mathbf{b}+\mathbf{s})]^{g_m}}{g_m!} \tag{3.3}$$

It's fairly easy to get the equation for $p(\mathbf{g}\,|\,H_0)$ too. We use $\overline{\mathbf{g}} = \mathbf{H}\mathbf{b}$ for the H_0. Then the resulting $LR(\mathbf{g})$ given by

$$LR(\mathbf{g}) = \frac{p(\mathbf{g}\,|\,H_1)}{p(\mathbf{g}\,|\,H_0)} = \prod_m e^{-[\mathbf{Hs}]_m}(1+\frac{[\mathbf{Hs}]_m}{[\mathbf{Hb}]_m})^{g_m}. \tag{3.4}$$

As is described in standard texts and articles (Metz, 1978), one can compute the ROC curve by forming a histogram of the $T(\mathbf{g}_-)$ responses, a histogram of the $T(\mathbf{g}_+)$ responses, and integrating each from T_0 to ∞. As $T_0 \to -\infty$, we sweep out the ROC curve. Digitally, we can obtain the $T(\mathbf{g}_+)$ histogram by generating $k = 1,...,N_{samp}$ values of $\mathbf{g}_+^k$ and evaluating $T(\mathbf{g}_+^k)$ and histograming it. Since each $\mathbf{g}_+^k$ has a different Poisson noise realization, we are sampling the likelihood. We can do the same for $T(\mathbf{g}_-^k)$, and then digitally integrate the two histograms to

sweep out the ROC curve. The resulting ROC curve is integrated numerically to get AROC. We need N_{samp} large enough to avoid sample error. We can use (Zoubir & Boashash, 1998) to ensure the sample error is acceptable. For the N_{samp} we use in experiments the error in AROC and areas under related curves such as LROC and AFROC is well under 1% (Zhou & Gindi, 2009).

How is all this to be used to find an optimal collimator? If we change the collimator, we change $\mathbf{H}$, and AROC changes. Thus the best collimator is the one that maximizes AROC ($\mathbf{H}$). We can illustrate this with a plot of AROC vs σ as seem in Figure 3.2. The collimator family is characterized by a depth-dependent FWHM via(2.3). We can choose a reference depth, say 10cm, and compute σ as the standard deviation of the Gaussian at 10cm. (Here we use $\sigma = FWHM / 2.355$) Then σ is a convenient index for collimators, and we can evaluate AROC(σ) instead of AROC($\mathbf{H}$).
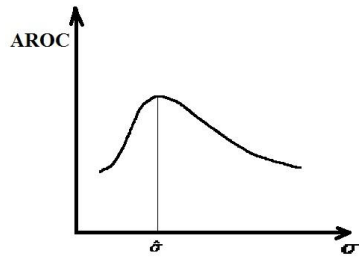
Figure 3.2 AROC vs. collimator as indexed by σ.
Here $\hat{\sigma}$ is the best collimator

Once again $T(\mathbf{g})$ is looking for the signal, but is doing this by examining $\mathbf{g}$, not a reconstruction $\hat{\mathbf{f}}$. In the $\mathbf{g}$-space, the signal appears as a blurry sinusoidal stripe, and that is what is being searched for by the IO, or any other observer, that examines the raw data.
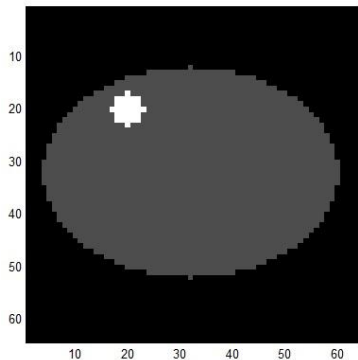
Figure 3.3 Image of Object $\mathbf{f}$
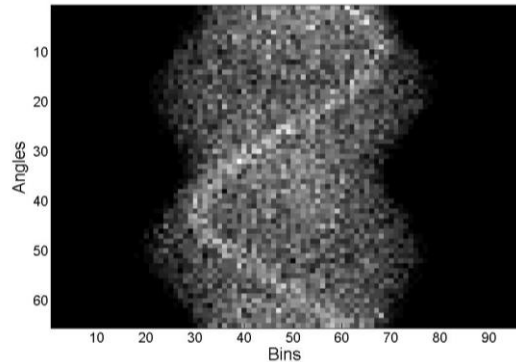
Figure 3.4 Projection Image $\mathbf{g}$ of $\mathbf{f}$ from Figure 3.3

The observer $T(\mathbf{g})$ tries to detect the presence of signal in the object space by its sinusoidal signature in the sinogram. The signal (bright spot) in Figure 3.3 causes the sinusoidal stipe in the noisy sinogram in Figure 3.4. The observer infers the presence of the signal $\mathbf{s}_j$ in the object space by looking for the sinusoidal pattern in the sinogram. In Figure 3.3, the signal has artificially high contrast for display purposes. In reality, the sinusoidal pattern due to $\mathbf{s}_j$ is buried in the noise.

The detection task we described is not realistic medically since it assumes that one knows where to look for the signal. Next we consider a more realistic LROC task.

3.3   LROC

The LROC task involves simultaneous detection and localization of a signal (Swensson, 1996). Localization means we estimate the signal location and correct localization means the estimate is within an error radius of the true signal. This circular region about the true signal is called the tolerance region and its radius is user specified. The LROC task assumes only one or zero signals per image. The localization part of the task is similar to the search procedure of a doctor scanning the image to look for something suspicious. Hence the LROC is more realistic that the ROC task, which involves detection only.

The LROC curve has as its abscissa the *FP* rate, the same as the ROC curve. The ordinate is CL, the correct localization rate, which is defined as the probability of simultaneously detecting a signal (if present) and localizing it within the tolerance region. The LROC curve is swept out as a tolerance T_0 is varied as we describe below. A typical LROC curve is shown in Figure 3.5. Note that the curve does not need to intersect the point (1,1).

The decision strategy for the LROC-IO maximizes ALROC, the area under the LROC curve. We summarize this decision strategy below. See (Khurd & Gindi, 2005) for the detailed derivation, which uses a modified Neyman-Pearson method.
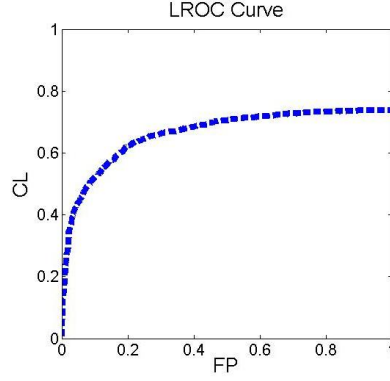
Figure 3.5 LROC

Let $\mathbf{j}$ be the location of the signal in $\mathbf{f}$, so that a signal present object is $\mathbf{f}_+ = \mathbf{b} + \mathbf{s}_j$ with $\mathbf{b}$ known as before and $\mathbf{s}_j$ a signal which varies only in location j. Clearly $\mathbf{f}_- = \mathbf{b}$ is for signal-absent objects. A signal present sinogram is then $\mathbf{g} = \mathbf{H}(\mathbf{b} + \mathbf{s}_j) + \mathbf{n}$ and signal absent sinogram is $\mathbf{g} = \mathbf{Hb} + \mathbf{n}$. Let $C(l)$ be the tolerance region about pixel l. There are L such regions, so $l = 1, ..., L$. The expression $j \in C(l)$ means that $\mathbf{s}_j$ lies within the tolerance radius about location l. We may define the likelihood $p(\mathbf{g} \mid H_0)$ as we did for the ROC case. Define H_l to be the hypothesis that a signal is located in a tolerance region $C(l)$ centered at $l = 1, ..., L$. The signal absent hypothesis H_0 is as before for the ROC case. Thus we have $L+1$ hypotheses. For a hypothesis that a signal is present at j, the likelihood is $p(\mathbf{g} \mid H_j)$. The likelihood ratio, analogous to $LR(\mathbf{g})$ for the ROC case, is $LR(\mathbf{g}, \mathbf{s}_j)$. In analogy to (3.4) $LR(\mathbf{g}, \mathbf{s}_j)$ is given by

$$LR(\mathbf{g}, \mathbf{s}_j) = \frac{p(\mathbf{g} \mid H_j)}{p(\mathbf{g} \mid H_0)} = \prod_m e^{-[\mathbf{Hs}_j]_m} (1 + \frac{[\mathbf{Hs}_j]_m}{[\mathbf{Hb}]_m})^{g_m} \qquad (3.5)$$

Now we can write the LROC ideal decision strategy:

$$\begin{aligned}
T(\mathbf{g}) &= \max_{l=\{1,...,L\}} \sum_{j \in C(l)} p(\mathbf{s}_j) LR(\mathbf{g} \mid \mathbf{s}_j) \\
l(\mathbf{g}) &= \arg\max_{l=\{1,...,L\}} \sum_{j \in C(l))} p(\mathbf{s}_j) LR(\mathbf{g} \mid \mathbf{s}_j) \\
&\textit{Decide } H_{l(\mathbf{g})} \textit{ if } T(\mathbf{g}) > T_0 \textit{ else decide } H_0.
\end{aligned} \qquad (3.6)$$

In (3.6), $p(\mathbf{s}_j)$ is the prior on signal location. As before $T(\mathbf{g})$ is the scalar observer response and is the maximum of an objective function. The objective function at each location l is a summation of the likelihood ratio (weighted by prior $p(\mathbf{s}_j)$) within the circular tolerance region. The decision strategy reports not only an observer response $T(\mathbf{g})$, but an estimated location of the signal $l(\mathbf{g})$, with $l(\mathbf{g})$ simply the location where $T(\mathbf{g})$ is maximized. Finally, we report signal present at $l(\mathbf{g})$ if $T(\mathbf{g}) \geq T_0$ and report signal-absent otherwise. The presence of the max operator, the summation, and the reporting of a response and location make this IO very different than the two-class decision strategy of (3.1).

Eq.(3.6) has a mechanical interpretation. Take $p(\mathbf{s}_j)$ to be uniform without loss of generality. Then one takes $\mathbf{g}$ (which may or may not have a signal at j) and converts it to a "pre-summation" image $LR(\mathbf{g},\mathbf{s}_j)$. The pre-summation image is indexed by j, one then convolves $LR(\mathbf{g},\mathbf{s}_j)$ with $C(j)$ to get a "post-summation" image $\sum_{j \in C(l)} p(\mathbf{s}_j) LR(\mathbf{g},\mathbf{s}_j)$ which is a function of spatial coordinate l. The max of the post-summation image and its $\arg\max$ are $T(\mathbf{g})$ and $l(\mathbf{g})$.

To compute ALROC we take N_{samp} $\mathbf{g}_+$ images (with $\mathbf{s}_j$ distributed as per $p(\mathbf{s}_j)$) and N_{samp} $\mathbf{g}_-$ images. For the $\mathbf{g}_-$ images we form histogram $T(\mathbf{g}_-)$. For the $\mathbf{g}_+$ images, we compare $l(\mathbf{g})$ with the true signal location j and see if $j \in C(l)$. If it is, we keep it, otherwise discard it since it is mislocalized. We form a histogram $T(\mathbf{g}_+)$ for the correctly localized responses. The area of $T(\mathbf{g}_-)$ is normalized to unity and the area of $T(\mathbf{g}_+)$ is normalized to a number equal to the proportion of correct localizations. As before, we sweep threshold T_0 from $+\infty \to -\infty$ and integrate $T(\mathbf{g}_-)$ from T_0 to $+\infty$ to get $FP(T_0)$ and integrate $T(\mathbf{g}_+)$ from T_0 to $+\infty$ to get $CL(T_0)$. This sweeps the LROC curve as seen in Figure 3.5. We can then use numerical integration to generate ALROC. Note there are three numerical integrations: one for $T(\mathbf{g}_+)$, one for $T(\mathbf{g}_-)$ and one for the LROC curve.

As in the ROC case, we can select a best collimator by seeing where the LROC vs. σ curve peaks. Previous work in our lab on LROC evaluation of simple pinhole systems was reported in(Zhou, Khurd, Kulkarni, Rangarajan, & G, 2008). Initial application of LROC, work also from our lab, to SPECT collimator optimization was reported in (Zhou & Gindi, 2009)

3.4   AFROC

The Free-response ROC (FROC) and the related Alternative FROC (AFROC) tasks deal with the detection and localization of *multiple* signals. In a 2-D image, a doctor sometimes notices more than one lesion, so the AFROC task is medically more realistic than the LROC task. We describe only the AFROC since the FROC is closely related. The abscissa of the AFROC curve is the probability that one or more false positive "reports" are made per image. The ordinate is the correct localization rate. To more precisely define these consider the images in Figure 3.6.
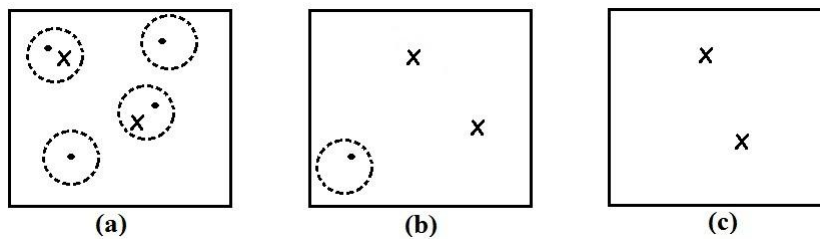
Figure 3.6 Images help define AFROC. A dot is a true signal with the circle, the tolerance region. The "X" is a "report", i.e. a place where the observer estimates a signal is present. See text for further explanation.

In the signal-present Figure 3.6 (a) there are two correct reports (an "X" inside the tolerance circle) and two missed signals (false negatives). In the signal-present Figure 3.6(b), there are two false positives (X's marks) and one false negative (unmarked true signal). In the signal-absent Figure 3.6(c), there are two false positives. In the images in Figure 3.6, we see that the percentage of images with false positive reports is 2/3. This percentage, or probability of at least one false positive per image, is the abscissa of the AFROC curve. We also note that of the five true signals in the 3 images, two are correctly detected and localized, so the CL rate for the 3 images is 2/5. The CL rate is the ordinate of the AFROC curve. As a threshold is swept the CL and FP rates vary and the AFROC curve is swept out. A typical AFROC curve is shown in Figure 3.7. The area under this curve we will call the AAFROC.
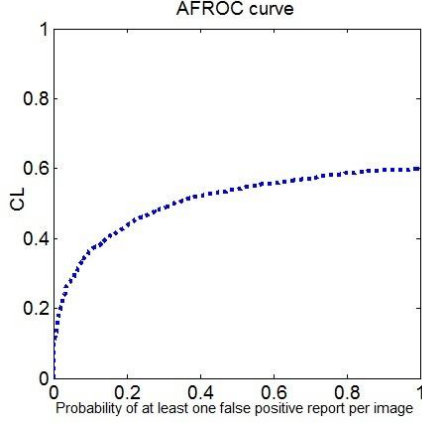
Figure 3.7 AFROC Curve

The IO for the AFROC task, the one that maximizes AAFROC, is non-intuitive. The derivation is given in (Khurd et al., 2010)and we summarize it here. We will use somewhat different notation than we did for the LROC case. In particular we will assume that the object is continuous not digital. (A continuous object is realistic). Then signal locations are denoted by a 2-D vector $\mathbf{r}$ and summations become integrals.

Let $\boldsymbol{\theta} = (n, \mathbf{r}_1, \mathbf{r}_2, \ldots, \mathbf{r}_n)$ be a vector summarizing the number (n) and locations of true signals, and $\hat{\boldsymbol{\theta}} = (\hat{n}, \hat{\mathbf{r}}_1, \hat{\mathbf{r}}_2, \ldots, \hat{\mathbf{r}}_{\hat{n}})$ summarize the estimated number $(\hat{n})$ and locations of signals. The likelihood ratio we need is (Liu, Khurd, & Gindi, 2010)

$$LR(\mathbf{g}, \boldsymbol{\theta}) = LR(\mathbf{g}; \mathbf{r}_1, \mathbf{r}_2, \ldots, \mathbf{r}_n) = \frac{p(\mathbf{g} \mid H_1, \mathbf{r}_1, \mathbf{r}_2, \ldots, \mathbf{r}_n)}{p(\mathbf{g} \mid H_0)} \tag{3.7}$$

Note that the numerator contains the hypothesis that n signals are present and are located at the listed positions. There is no order to the $\mathbf{r}_i$'s. If you permute them, the likelihood stays the same.

The optimal decision strategy is then formulated as the max of an objective function (Khurd et al., 2010)

$$\Phi(g;\tilde{\boldsymbol{\theta}}) = \int d\boldsymbol{\theta} p_{\boldsymbol{\theta}}(\boldsymbol{\theta}) LR(\mathbf{g};\boldsymbol{\theta}) u(\boldsymbol{\theta};\tilde{\boldsymbol{\theta}})$$

$$T(\mathbf{g}) = \max_{\tilde{\boldsymbol{\theta}}} \Phi(\mathbf{g};\tilde{\boldsymbol{\theta}})$$

$$\hat{\boldsymbol{\theta}} \equiv (\hat{\mathbf{r}}_1, \hat{\mathbf{r}}_2, \ldots, \hat{\mathbf{r}}_{\hat{n}}) = \arg\max_{\tilde{\boldsymbol{\theta}}} \Phi(\mathbf{g};\tilde{\boldsymbol{\theta}})$$

Decide $\hat{n}$ signals at locations $\hat{\mathbf{r}}_1, \hat{\mathbf{r}}_2, \ldots, \hat{\mathbf{r}}_{\hat{n}}$ if $T(\mathbf{g}) > T_0$, else decide signal $-$ absent.

where

$$u(\boldsymbol{\theta};\tilde{\boldsymbol{\theta}}) \equiv u(n, \mathbf{r}_1, \ldots, \mathbf{r}_n; \tilde{\mathbf{r}}_1, \ldots, \tilde{\mathbf{r}}_{\tilde{n}}) = \frac{1}{n}\{\sum_{m=1}^{n} step[\sum_{m'=1}^{\tilde{n}} circ(\frac{|\tilde{\mathbf{r}}_{m'} - \mathbf{r}_m|}{R})]\}.$$

$$(3.8)$$

where $p_{\boldsymbol{\theta}}(\boldsymbol{\theta})$ is the prior on true signals, $T(\mathbf{g})$ and T_0 are the detection observer report and threshold, respectively, and R the radius of the tolerance region. The "utility" function $u(\boldsymbol{\theta};\tilde{\boldsymbol{\theta}})$ counts the percentage of correctly localized signals.

Mechanically, the decision strategy takes each $\mathbf{g}$ of a large sample set, and computes a candidate response Φ by exploring all "constellations" $\tilde{\boldsymbol{\theta}}$ of candidate responses[1]. So let's say $n = 3$ and $\hat{n}$ is fixed at 3 and the image is 100×100. Then we need explore $(100 \times 100)^3$ $\tilde{\boldsymbol{\theta}}$'s for each $\mathbf{g}$, or 10^7 hypotheses per $\mathbf{g}$! One takes the max to get $T(\mathbf{g})$ and the arg max to get $\hat{\boldsymbol{\theta}}$ for each $\mathbf{g}$. The $T(\mathbf{g})$ are formed into appropriate histograms for $\mathbf{g}_+$ and $\mathbf{g}_-$ and the AFROC curve swept by integrating from T_0 to $+\infty$. (We shall give more detail in a later chapter).

The IO in (3.8) makes a reasonable approximation that the *FP* rate is computed from signal-absent images only. We note that in (Clarkson, 2007) the AFROC detection-localization ideal decision strategy was generalized to an ideal decision strategy for detecting and estimating *anything*!! For example, one could detect multiple signals and jointly estimate their radii. All that is needed is a redefinition of the utility function. The resulting curve is termed the EROC (Estimation ROC) curve and it is easy to show an IO that maximizes the EROC area.

Above it was shown that the search involved in maximizing Φ is intractable. However, under certain approximations (Liu et al., 2010), the decision strategy in (3.8) can be computed much more quickly. The main requirements are that $p_{\boldsymbol{\theta}}(\mathbf{r}_1, \ldots, \mathbf{r}_n)$ and $LR(\mathbf{g} \mid H_1, \mathbf{r}_1, \mathbf{r}_2, \ldots, \mathbf{r}_n)$ be separable in $\mathbf{r}_i$ and that the signals be further apart than $2R$.

---

[1] Each $\tilde{\boldsymbol{\theta}}$ is like a stellar constellation of points.

We now have defined the IO for the LROC and FROC tasks. In the next three chapters, we apply them to SPECT collimator optimization.

Chapter 4

LROC Experiments with Planar Imaging

4.1 Introduction

In the next 3 chapters we apply LROC, AFROC to medical imaging. Note there is a long history of pure detection AROC studies(Barrett & Myers, 2003) which we do not consider here. But we note LROC optimization is compared to ROC optimization in (Zhou et al., 2008)

We first explored planar imaging instead of SPECT since this is easier computationally. We have already introduced planar imaging in Chapter 1, section 4, which is basically one angle object-image parallel projection. In our experiment, we use 2-D planar object with a fixed distance (d) to the image plane. Note that the object $\mathbf{f}$ is itself planar (2-D) here. This is not realistic, but is convenient for the initial experiments we describe in this chapter. The planar projection geometry is shown in Figure 4.1. Note that the image $\mathbf{g}$ appears right behind the collimator, but in Figure 4.1 it is shown at a distance from the collimator just for display purposes. In the middle of Figure 4.1 is the collimator, labeled appropriately as $\mathbf{H}$.
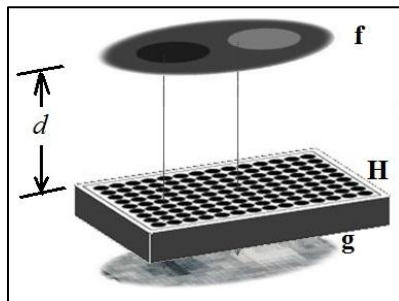
Figure 4.1 Planar Imaging Projection Model

Mathematically, the image can be described as

$$\mathbf{g} = \mathbf{H}\mathbf{f} + \mathbf{n} \tag{4.1}$$

where $\mathbf{f}$ represents the source to be determined and $\mathbf{n}$ represents the radiation noise which is Poisson distributed. $\mathbf{H}$ is the system matrix which summarizes many physical effects of the

transfer of photons to the detector. But here $\mathbf{H}$ will be needed only to model the collimator. The $\mathbf{g}$ is the projection data.

Since d is fixed, the depth-dependent point-spread function (psf) described in Chapter 3 becomes a space invariant psf, so $\mathbf{Hf}$ becomes a convolution instead of a matrix-vector operation. Thus, we can rewrite (4.1) as

$$\mathbf{g} = \mathbf{f} * \mathbf{h} + \mathbf{n} \tag{4.2}$$

where $*$ stands for 2-D convolution and $\mathbf{h}$ is the psf.

Our goal is to optimize the collimator. The collimator here is modeled much more simply than in Chapter 2, which was more realistic in physics. We model the collimator here simply as a 2-D Gaussian kernel of unit height and standard deviation σ. Note that efficiency here is area under Gaussian psf curve and resolution is σ. Thus efficiency goes as $\sim \sigma^2$ and resolution as $\sim \sigma$. In our experiment, $\mathbf{h}$ is sampled on a 21×21 pixel grid and σ varies from 0.1 to 3.0 in units of pixels. The sample values are calculated by integrating the Gaussian psf over a pixel.

Our goal is to apply, for the LROC task, the ideal observer (IO) and also apply a suboptimal observer on the ensemble of $\mathbf{g}$ images to find ALROC vs. σ curves for each case. Then we can determine if suboptimal observers give a significantly different ALROC curve. Intuitively, one might think that scanning a simple empirical observer and taking a max directly will yield an ALROC vs σ curve with same argmax as that of the IO. If that is true, then using the suboptimal observer might be much computationally easier than using the IO. However, experimental results will show that the IO acts differently than an empirical observer.

4.2   Imaging details
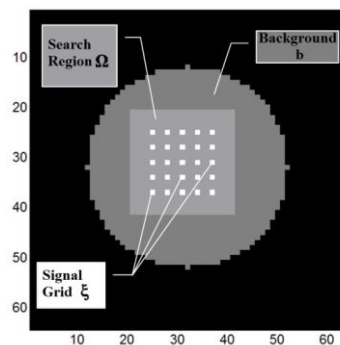
Figure 4.2 The Planar Object

As seen in Figure 4.2, our planar object background is circular with radius equal to 20 pixels from center pixel (32, 32). The entire object plane is the 64×64 black region as shown in Figure 4.2. The gray square in Figure 4.2 is the search region $\mathbf{\Omega}$ (21×21 centered at (32,32)), which covers the area in which we search for a signal. In other words, $\mathbf{\Omega}$ is the region over which we take a max of the post-summation image. The one-pixel white spots are our signal grid ξ, which include all the true signal locations we may put a signal on (from (25,25), step equally by 3 pixels , totally 25 spots). Note that ξ and $\mathbf{\Omega}$ need not be the same. The locations ξ are where true signals might appear in $\mathbf{f}_+$ and the search region $\mathbf{\Omega}$ contains hypothesized locations. One could make ξ a single pixel, $\mathbf{\Omega}$ an extended region, and still have a valid LROC simulation.

The mean count level in $\mathbf{g}$ is simply determined by $\mathbf{g} = \mathbf{f} * \mathbf{h}$, so in the background where $\mathbf{b} = 100$, if area of $\mathbf{h}$ is 2.5, then the background region in $\mathbf{g}$ is 250. This simply says that the integral of $\mathbf{g}$ is the integral of $\mathbf{f}$ times the integral of $\mathbf{h}$. If the collimator is efficient, then the integral of $\mathbf{h} > 1$. The dimensions of $\mathbf{g}$ are 84×84 since regular non-circular convolution is used. One particular $\mathbf{h}$ is shown in Figure 4.3 and its central profile in Figure 4.4. One $\mathbf{g}$ is shown in Figure 4.5. In Figure 4.5, signal is blurred by $\mathbf{h}$ and masked by noise.
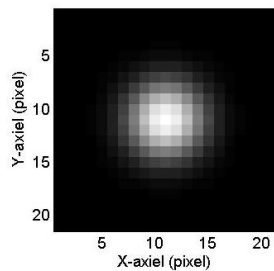
Figure 4.3 h kernel image($\sigma = 2.5$)
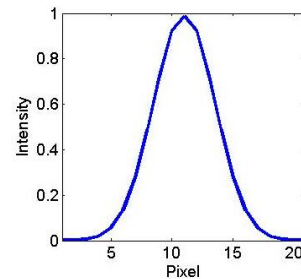
Figure 4.4 h kernel ($\sigma = 2.5$) central profile
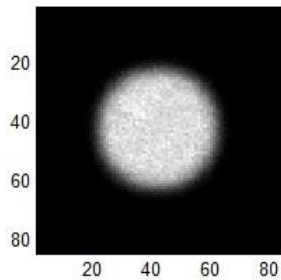
Figure 4.5 g image with signal present at (25,25) in object space($\mathbf{f}$-space)
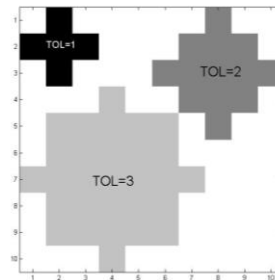
Figure 4.6 TOL templates

4.3   LROC experiment

The IO is given by (3.6) with $LR(\mathbf{g}, \mathbf{s}_j)$ given by (3.5) with $\mathbf{Hx}$ interpreted as $\mathbf{h} * \mathbf{x}$ for vector $\mathbf{x}$. The prior $p(\mathbf{s}_j)$ is a uniform distribution over ξ. The tolerance region $C(l)$ of radius TOL is defined digitally by including those pixels $\leq$ distance TOL (in pixel units) away from a central pixel. TOL templates shown in Figure 4.6.

To generate $\mathbf{g}_+$ (signal present) images, we first generate $\mathbf{f}_+$ according to the ξ ($\mathbf{f}_+ = \mathbf{b} + \mathbf{s}_i$, i indexes signal location from ξ), then convolve $\mathbf{f}_+$ with $\mathbf{h}$ and then add Poisson noise to obtain one sample $\mathbf{g}_+^k$, where k indexes sample number. We accumulate N_{samp} $\mathbf{g}_+$ by using $\mathbf{f}_+$ according to different signal locations from ξ. For each location in ξ, we generate an equal number of signals. Note that signal locations are not generated by sampling a uniform distribution $p(\mathbf{s}_j)$. Uniform sampling would be a more correct way of simulating $\mathbf{g}_+$, but using an equal number of samples at each $i \in \xi$ is a good approximation. For $\mathbf{g}_-$ generation, the only difference is we use $\mathbf{f}_- = \mathbf{b}$ directly as the object.

After accumulating N_{samp} $\mathbf{g}_+$ and $\mathbf{g}_-$, we apply observer T on $\mathbf{g}$ as introduced in Chapter 3 to get $T(\mathbf{g}_+)$ and $T(\mathbf{g}_-)$. We then accumulate histograms for $T(\mathbf{g}_+)$ and $T(\mathbf{g}_-)$ and follow the "scoring" procedure (i.e. integrating the normalized histograms to get LROC curve then integrating the LROC curve to get ALROC scalar value). This yields the ALROC vs. σ curve shown in Figure 4.7.
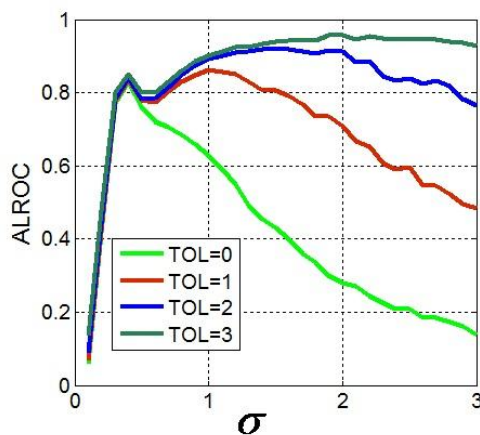
Figure 4.7 ALROC vs. σ for IO

Comments on Figure 4.7:

a) ALROC rises with TOL as expected.

b) At very small σ, ALROC is low due to high noise.

c) At very high σ, ALROC is low because blur inhibits localization. However, with TOL large, ALROC remains large.

d) Optimal σ is around $\sigma = 0.3$ for small tolerance and shifts rightward with higher tolerance.

Note: if $TOL \to \infty$, we get a pure detection problem with signal location unknown, and the best $\sigma \to \infty$. So if we are doing detection only, the best collimator has infinitely large holes! This paradox for detection problems was observed in (Myers, 1990) though in that case the signal location was known.

4.4 Suboptimal observer experiment

IO is a scanning observer that takes a max, but the IO can be difficult to compute if likelihoods are hard to evaluate. Can we simply scan an empirical simple observer, then take the max and get a ALROC vs. σ curve similar to IO, or at least one that yields same σ^* ($\sigma^* = \arg\max_{\sigma} ALROC(\sigma)$).

We tried this. We took the empirical observer to be a scanning matched filter (SMF). A matched filter is defined in (Kay, 1998) and turns out to be, for our case, a j-dependent (hence scanning) observer:

$$T(\mathbf{g}, \mathbf{s}_j) = (\bar{\mathbf{g}}_{+,j} - \bar{\mathbf{g}}_-)^T \mathbf{g} = (\mathbf{h} * \mathbf{s}_j)^T \mathbf{g} \tag{4.3}$$

where the observer itself is $\mathbf{h} * \mathbf{s}_j$ and the observer response an inner product of the observer at j with $\mathbf{g}$. Rationale: for flat $\mathbf{f}$, Poisson distribution looks like iid Gaussian distribution except at the signal. For iid Gaussian, the IO for a detection-only problem is a matched filter which is a likelihood ratio, but as most people do, we take log likelihood $\log(LR)$ (but we can't do this log step in our IO). Under Gaussian approximation of Poisson and $\log(LR)$, and scan feature where the MF evaluated at each j, we get (4.3).

31

Basically, the LROC-IO becomes a SMF by 3 steps:

- Cancel the summation over tolerance region step
- take log, which LROC-IO does not. That is, we cannot take a log right before the exp in (3.5).
- Use Gaussian noise for *LR* instead Poisson.

As the same way in section 4.3, we obtain N_{samp} $\mathbf{g}_+$ and $\mathbf{g}_-$. For one particular $\mathbf{g}_+$ for example, we apply SMF over it by(4.3), as j indexes each location among $\mathbf{\Omega}$ and store $T(\mathbf{g})$ and take the max value of it and record the location j^* as the guessed signal-present location. We do it for each $\mathbf{g}_+$ and then score ALROC as we did for IO.

Then, we get
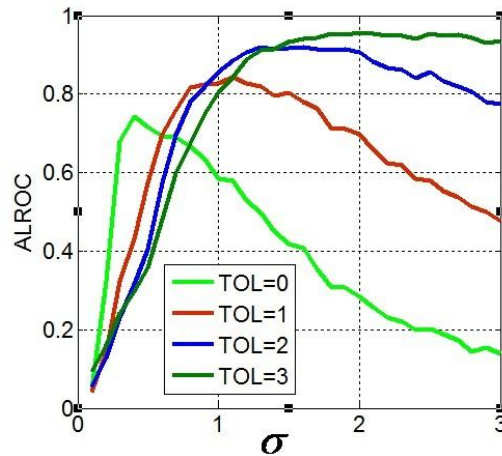
Figure 4.8 ALROC vs. σ for SMF

Comments on Figure 4.8: ALROC curves here are very different than Figure 4.7 for IO. Here, curves show "crossover" which means at some σ, small TOL's ALROC is larger than big TOL. So we see that substitution of a reasonable empirical observer yields very different results than the true ideal observer. At larger σ, the SMF curves do match the IO curves pretty well however. Further investigation is needed.

Chapter 5

LROC Experiments with SPECT

5.1   Introduction

In chapter 4, we have explained LROC experiments with planar imaging of a planar object. Here, we consider a medically more realistic task, the joint detection and localization of one signal in one 2-D slice in SPECT. We use an ideal observer (Eq.(3.5)& Eq.(3.6)) to optimize collimator design. The ideal observer operates on the sinogram data. We consider a family of parallel-hole hexagonal collimators of varying resolution and efficiency and optimize over this set. This experiment is similar to previous work in our lab (Zhou & Gindi, 2009). In the previous work, Zhou obtained artifactual results due to an overly large search region (Ω). Zhou's Ω and her object was the whole object space (64×64 pixels), which is unrealistic for a real clinical case. In a clinical image, the interested organ is always relatively small compared to the whole image. Since SPECT is highly space variant due to depth-dependent blur and attenuation, signals approaching the edge of the object are more easily seen. Zhou demonstrated that ALROC was much greater if the search was constrained to a region near the outer border of Ω. Thus, in our experiment, we decide to use a smaller search region which makes the region quasi-space invariant. It is more realistic than Zhou's work. Zhou also obtained results showing that extreme collimators of wide bore and very high efficiency were best. This seemed unintuitive given the localization task.

In this experiment, we focus on 2-D SPECT imaging, which is basically one 2D slice object viewed from the "side" by the collimator. Since in clinical case, doctors tend to view one slice of a 3-D reconstruction at any one moment, our experiment is clinically valid. Our 2-D SPECT object is shown in Figure 1.8. Thus the object was viewed "edge-on" and projections $\mathbf{Hf}$ were calculated at many angles. The code for projection is quite complex and we used MIPL-Sim. MIPL-Sim is a large C package written over many years in our lab. It simulates SPECT projection and reconstruction.

Our goal once again is to optimize the collimator via finding argmax of ALROC (σ) curve. As discussed in Chapter 3 (Figure 3.3, Figure 3.4), the observer detects the signature of the signal in the sinogram space.

5.2   Imaging details

As stated in Chapter 2, the imaging equation for SPECT is

$$\mathbf{g} = \mathbf{Hf} + \mathbf{n} \tag{5.1}$$

Here, the $\mathbf{H}$ matrix modeled depth dependent blur as discussed in Chapter 2 (Figure 2.6), but we did not model attenuation effects.
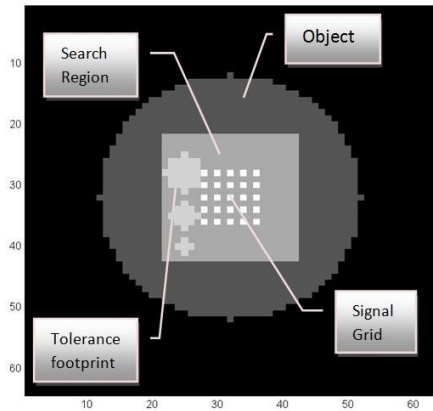
Figure 5.1 The SPECT Object. The tolerance
footprints are superimposed on the object

As seen in Figure 5.1, our SPECT object background is circular with radius equal to 20 pixels from the center pixel (32, 32). The entire object plane is the 64×64 black region as shown in Figure 5.1. The gray square is the search region $\mathbf{\Omega}$ (21×21 centered at (32,32)), which covers the area in which we search for a signal. In other words, $\mathbf{\Omega}$ is the region over which we take a max of the post-summation image. The one-pixel white spots are our signal grid ξ, which include all the true signal locations we may put a signal on (from (28,28), step equally by 2 pixels , totally 25 spots). The signal intensity is 6 times that of the background. Note that ξ and $\mathbf{\Omega}$ need not be the same. The locations ξ are where true signals might appear in $\mathbf{f}_+$ and the search region $\mathbf{\Omega}$

34

contains hypothesized locations. One could make ξ a single pixel, Ω an extended region, and still have a valid LROC simulation. The tolerance footprints are also shown in Figure 5.1, from top to bottom, the radiuses are 3, 2 and 1.

In our simulation, our physical pixel size is 0.625cm, and our bin size is also 0.625cm (shown in Figure 3.4). The distance from the object center (32,32, in pixel) to imaging plane is 35cm, We apply 65 equispaced angles over 2π around the object. The bin-number, that is the number of detectors in the gantry at any one angle, is 96, which is designed wide enough to capture all possible photons emitting from the object. In our experiment, we set count level equal to 30,000. That is, the mean number of counts in a sinogram was 30,000. We used this clinically realistic number for one reference collimator, the GAP (General All Purpose) collimator which corresponds to an actual collimator. For other collimators the mean count level was scaled by efficiency relative to the GAP.

We have introduced the collimator models in Chapter 2, including definitions of average efficiency, FWHM, etc. Again, $FWHM(d) = \sqrt{\left(\dfrac{D}{l}d\right)^2 + (2.35\sigma_0)^2}$ (2.3), where FWHM is the Full Width at Half Max of the psf, and d is the distance from source to the crystal face, σ_0 is the intrinsic resolution, which is equal to 0.15cm. In our SPECT simulation experiments, we use a hexagonal bore shape, and thus $D=1.819S$, where S is the length of one of the hexagonal sides, as shown in Figure 2.9. Here, we have (Wernick & Aarsvold, 2004) $SPT = HOLSEP - \dfrac{\sqrt{\pi}}{\sqrt[4]{12}}D$.

With all these definitions, the average (over point source position) collimator efficiency for a hexagonal lattice is given by Eq.(2.4). A typical value of average efficiency is about 2×10^{-4}. With (2.3) and (2.4) together, we can characterize the collimator. Eq.(2.3) is a measure of resolution and (2.4) a measure of noise behavior. (A more efficient collimator collects more photons and so has less relative noise). We selected a family of 10 collimators to span a resolution-efficiency tradeoff. We looked for the collimator that yields the best performance among the 10 collimators. These collimators are presumed to be made of lead and we assume a photon energy, 140 keV, which is completely blocked by the lead.

We show the tradeoff in Figure 5.2**,** and Table 5.1 summarizes the collimator parameters. The UHR (ultra high resolution). HR (high resolution), GAP (general all purpose) and UHSens

(ultra high sensitivity) collimators are real collimators used for clinical purposes. The C1,..., C6 collimators are simulated ones which designed to span the resolution-efficiency curve. The last column of the table lists efficiency relative to that of the GAP collimator. We note that in our simulations, we assume a monoenergetic 140 keV Tc-99 m source. This radionuclide is commonly used in the clinic.
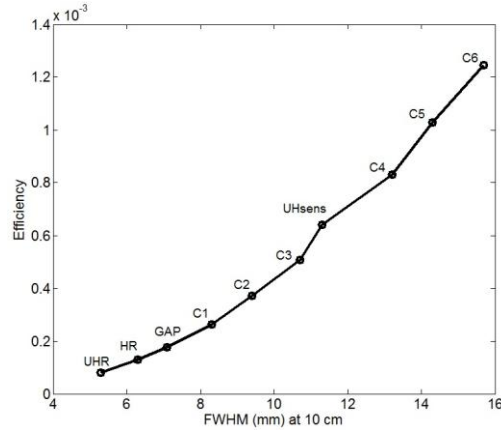
Figure 5.2 Efficiency versus FWHM for our collimator family. This is a noise-resolution curve

Table 5.1 Parameters for the proposed collimator family.

Collimator type	Bore diameter (mm)	Bore length (mm)	Septal thickness (mm)	FWHM (mm) at 10 cm	Relative efficiency
UHR	1.40	34.9	0.15	5.3	0.46
HR	1.40	27.0	0.18	6.3	0.74
GAP	1.57	25.4	0.24	7.1	1.00
C1	1.90	25.4	0.28	8.3	1.50
C2	2.22	25.4	0.28	9.4	2.10
C3	2.55	25.4	0.28	10.7	2.80
UHsens	2.84	25.4	0.28	11.3	3.70
C4	3.20	25.4	0.28	13.2	4.60
C5	3.53	25.4	0.28	14.3	5.80
C6	3.86	25.4	0.28	15.7	7.00

5.3   LROC experiment

To generate $\mathbf{g}_+$ (signal present) images, we first generate $\mathbf{f}_+$ (our signal intensity is 6 times of the background) according to the ξ ($\mathbf{f}_+ = \mathbf{b} + \mathbf{s}_i$, i indexes signal location from ξ), then use MIPL-Sim to simulate the SPECT imaging (with Poisson noise) acquisition to obtain one sample $\mathbf{g}_+^k$, where k indexes sample number. We accumulate N_{samp}^+ $\mathbf{g}_+$ by using $\mathbf{f}_+$ according to different signal locations from ξ. For each location in ξ, we generate an equal number of signals. Note that signal locations are not generated by sampling a uniform distribution $p(\mathbf{s}_i)$. Uniform sampling would be a more correct way of simulating $\mathbf{g}_+$, but using an equal number of samples at each $i \in \xi$ is a good approximation. For $\mathbf{g}_-$ generation, the only difference is we use $\mathbf{f}_- = \mathbf{b}$ directly as the object. In our experiment, our N_{samp}^+ for $\mathbf{g}_+$ is 2,000 and N_{samp}^- for $\mathbf{g}_-$ is 1,000. We used more signal present samples because mislocalized observer location estimates are excluded from the histogram. Thus of the 2,000 signal-present responses, only a fraction make it to the $T(\mathbf{g}_+)$ histogram.

After accumulating N_{samp}^+ $\mathbf{g}_+$ and N_{samp}^- $\mathbf{g}_-$, we apply the ideal observer T on $\mathbf{g}$ as introduced in Chapter 3 to get $T(\mathbf{g}_+)$ and $T(\mathbf{g}_-)$. The observer responses are accumulated in histograms for which we also use the notation $T(\mathbf{g}_+)$ and $T(\mathbf{g}_-)$. Meantime, we also get the correct-localized samples $CL(g)$. That is, for each $\mathbf{g}_+^k$, we examine the estimated location $l(\mathbf{g}_+^k)$ to see if it is within a tolerance radius of the true signal location. If is, we mark the sample number as valid and include those samples in the histogram $T(\mathbf{g}_+)$. Invalid localizations are marked and the corresponding observer responses are excluded from $T(\mathbf{g}_+)$. We then accumulate histograms for $T(\mathbf{g}_+)$ and $T(\mathbf{g}_-)$ and follow the "scoring" procedure (i.e. integrating the normalized histograms to get LROC curve then integrating the LROC curve to get ALROC scalar value) mentioned in Chapter 3.

Mathematically, our observer can be described in (3.5) and (3.6). From coding point of view, some programming tricks are applied below:

a) For (3.5), $[\mathbf{Hs}_j]_m$, $[\mathbf{Hb}]_m$ and $e^{-[\mathbf{Hs}_j]_m}$ can be pre-computed, avoiding repeating computation for each sample.

b) In scoring work, since the $T(\mathbf{g}_+)$ and $T(\mathbf{g}_-)$ are in a huge range, we take $\log(T(\mathbf{g}_+))$ and $\log(T(\mathbf{g}_-))$ and then histogram them. Log transformation is monotonic, thus we won't lose any information but get nice histograms shown in Figure 5.3. That is, if one integrates $T(\mathbf{g}_-)$ and $T(\mathbf{g}_+)$ from T_0 to $+\infty$, the resulting integration is unchanged if we monotonically transform $T(\mathbf{g}_-)$ and $T(\mathbf{g}_+)$ before integration. Taking the log here is very different than taking the log of the likelihood ratio.

Figure 5.3 Collimator UHsens, TOL=3's histograms

5.4   Results

Figure 5.5 plots performance, in terms of ALROC, versus collimator resolution, FWHM. The abscissa indexes the collimator choice by its resolution FWHM for a source at depth 10 cm. Reference to Figure 5.2 relates this FWHM to efficiency. The curves in Figure 5.5 are indexed by tolerance. The lowest curve, labeled TOL=0, corresponds to perfect localization, which is sort of unrealistic for a SPECT blurred image. The TOL=3 case is also unrealistic at the other extreme of large tolerance. The TOL=2 case is the most realistic. For any tolerance, we can see

the peak shows up at collimator UHsens. As expected, ALROC performance goes north as localization becomes freer. Figure 5.5 shows that adding a localization restriction results, for the optimal collimator, in a finite collimator resolution. If there were no localization requirement, the ALROC curves would keep rising as FWHM increases, approaching unity. This was observed by (Zhou & Gindi, 2009) and is consistent with (Myers, 1990). We observe the optimal collimator to be UHsens. The conventional collimator for this study is the GAP. The vertical lines in Figure 5.5 highlight the GAP vs. the UHsens performance. Thus, a more efficient lower resolution collimator the UHsens, would be selected vs. the GAP according to this result. Our result is quite different from (Zhou & Gindi, 2009), which gave only rising curve with bigger collimator and no peaks showed up. We believe Zhou's paradoxical 'gaping aperture' is due to the unrealistic giant Ω. She obtained this result even though she had a localization requirement. In our experiment, TOL=2,3 are more realistic than too stringent TOL. So our final conclusion for the doctors is this: For certain clinical studies, replace your GAP collimator with another collimator, the UHsens, that yields blurrier sinograms with less relative noise.
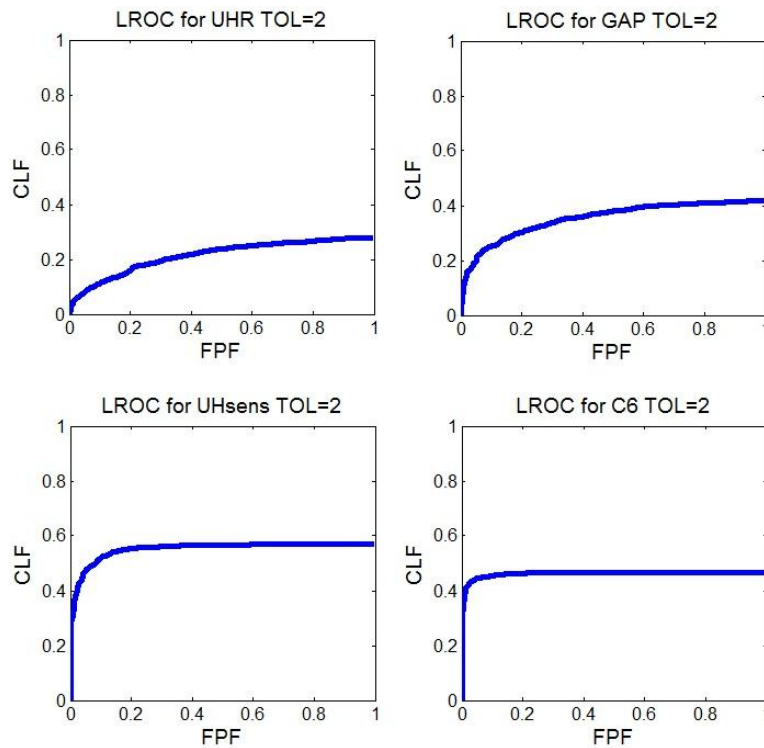
Figure 5.4 Representative LROC curves from the study
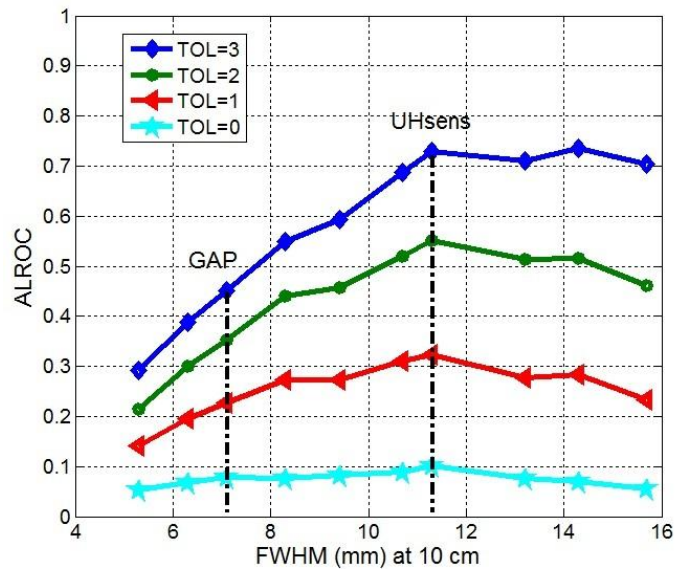
Figure 5.5 See text for explanation

Chapter 6
AFROC Experiments with SPECT

6.1   Computationally tractable version of AFROC ideal observer

In Chapter 3 we presented the ideal decision strategy (Eq.(3.8)) for the AFROC ideal observer, and also showed that the computation of the observer response was computationally difficult. In (Liu et al., 2010), our lab showed that under certain assumptions, the computation, in Eq.(3.8) could be done more rapidly. We summarize the work in (Liu et al., 2010), using the notation from Section 3.4.

First, we assume that there will be a finite number $\hat{n}$ of reports. In practice, a physician may typically mark 2 or 3 suspicious locations in a SPECT slice. It turns out that if the IO is restricted to making *up to* $\hat{n}$ reports, it will end up reporting *exactly* $\hat{n}$ reports (if the threshold T_0 is exceeded). While the true number of signals n can be variable, we'll reasonably assume that if signals are present, then exactly $n = 2$ signals will be present. In this case, it makes sense to set $\hat{n} = 2$. We call this the "2-2" case: Either zero or two signals are present (0 in $\mathbf{g}_-$, 2 in $\mathbf{g}_+$) and exactly two reports are made if a threshold is exceeded.

The next assumption is that the location prior is independent so that for the 2-2 case $p(\mathbf{r}_1, \mathbf{r}_2) = p(\mathbf{r}_1) p(\mathbf{r}_2)$. This independence in subject to restriction that the two signals be more than $2R$ apart, with R the tolerance radius. The next assumption is that the likelihood ratio is separable. For the 2-2 case, this means:

$$LR(\mathbf{g}; \mathbf{r}_1, \mathbf{r}_2) = (Constant)LR(\mathbf{g}; \mathbf{r}_1)LR(\mathbf{g}; \mathbf{r}_2) \tag{6.1}$$

If these assumptions hold then we can rapidly compute the IO. Now we show the fast algorithm. Define

$$J_1(\mathbf{g}) = \int p(\mathbf{r})LR(\mathbf{g}; \mathbf{r})d\mathbf{r} \tag{6.2}$$

where we can drop the subscript on $\mathbf{r}$ since we are integrating. Eq.(6.2) is equivalent to taking the LROC "pre-summation image" (described in Chapter 3) and integrating it. Next define

$$J_2(\mathbf{g},\tilde{\mathbf{r}}) = \int p(\mathbf{r})LR(\mathbf{g},\mathbf{r})circ\frac{|\tilde{\mathbf{r}}-\mathbf{r}|}{R}d\mathbf{r} \qquad (6.3)$$

Eq.(6.3) is equivalent to computing the LROC "post-summation image" (here written in continuous notation) of Chapter 3. For the 2-2 case, the objective function $\Phi(\mathbf{g},\hat{\boldsymbol{\theta}})$ of Eq.(3.8) then becomes

$$\Phi(\mathbf{g};\tilde{\mathbf{r}}_1,\tilde{\mathbf{r}}_2) = [J_2(\mathbf{g},\tilde{\mathbf{r}}_1) + J_2(\mathbf{g},\tilde{\mathbf{r}}_2)](J_1(\mathbf{g})) \qquad (6.4)$$

The $J_1(\mathbf{g})$ term can be pre-computed for a given $\mathbf{g}$. The term in brackets $[J_2(\mathbf{g},\tilde{\mathbf{r}}_1) + J_2(\mathbf{g},\tilde{\mathbf{r}}_2)]$ apparently tells us that we must search the $(\tilde{\mathbf{r}}_1,\tilde{\mathbf{r}}_2)$ space to find a particular $(\hat{\mathbf{r}}_1,\hat{\mathbf{r}}_2)$ that maximizes the sum in the brackets. This combinational search seems hard until one realizes that no search is needed. All one needs is the first two order statistics of $J_2(\mathbf{g},\tilde{\mathbf{r}})$, that is the $\hat{\mathbf{r}}_1$ that yields the max value of $J_2(\mathbf{g},\tilde{\mathbf{r}})$ and the $\hat{\mathbf{r}}_2$ value that yields the 2nd-highest value of $J_2(\mathbf{g},\tilde{\mathbf{r}})$. This choice of $(\hat{\mathbf{r}}_1,\hat{\mathbf{r}}_2)$ is guaranteed to maximize the term in brackets in (6.4) and hence maximize $\Phi(\mathbf{g};\tilde{\mathbf{r}}_1,\tilde{\mathbf{r}}_2)$ over $\tilde{\mathbf{r}}_1,\tilde{\mathbf{r}}_2$. One last restriction is that $\hat{\mathbf{r}}_1$ and $\hat{\mathbf{r}}_2$ must be separated by $2R$. Once we have $(\hat{\mathbf{r}}_1,\hat{\mathbf{r}}_2)$, then

$$\begin{aligned} T(\mathbf{g}) &= (J_2(\mathbf{g},\hat{\mathbf{r}}_1) + J_2(\mathbf{g},\hat{\mathbf{r}}_2))(J_1(\mathbf{g})) \quad and \\ \hat{\boldsymbol{\theta}} &= \hat{\mathbf{r}}_1,\hat{\mathbf{r}}_2 \end{aligned} \qquad (6.5)$$

as our IO observer report on $\mathbf{g}$.

The J_1, J_2 formulation has an easy mechanical interpretation. For a given $\mathbf{g}$, first take the pre-summation image and integrate it to get the $J_1(\mathbf{g})$ term. Then scan the LROC post summation image and locate the 1st max $\hat{\mathbf{r}}_1$ and 2nd max $\hat{\mathbf{r}}_2$, while ensuring $\| \hat{\mathbf{r}}_1 - \hat{\mathbf{r}}_2 \| \geq 2R$. Then plug these $\hat{\mathbf{r}}_1,\hat{\mathbf{r}}_2$ into (6.5) and multiply by $J_1(\mathbf{g})$ to get the observer report. In sum, combinational search becomes sequential search + order statistics.

6.2 Scoring the AFROC observer reports

We need to come up with scoring procedure consistent with the definitions of AFROC. Let's say we have scanned $k = 1, 2..., N_{samp}$ signal present images to yield $(T(\mathbf{g}_+^k), \hat{\mathbf{r}}_1^k, \hat{\mathbf{r}}_2^k)$. If both $\hat{\mathbf{r}}_1^k$ and $\hat{\mathbf{r}}_2^k$ are further than the tolerance radius R from either of the true signals at $\mathbf{r}_1$ and $\mathbf{r}_2$, as depicted in Figure 6.1(b), then we have incorrect localization and the report is discarded (as we did for the LROC case). If *both* $\hat{\mathbf{r}}_1$ and $\hat{\mathbf{r}}_2$ are within R, as in Figure 6.1(a), then that $T(\mathbf{g}_+)$ is included in the histogram. If *one* of the two reports $\hat{\mathbf{r}}_1, \hat{\mathbf{r}}_2$ is within R of a true signal as in Figure 6.1(c), then it turns out that the correct scoring is to include the $T(\mathbf{g}_+)$ in the histogram, but to weight that histogram by $1/2$. In summary, let's say that

$$N_{samp} = N_{samp2} + N_{samp1} + N_{samp0}$$

where N_{samp2} cases have 2 correct localizations, N_{samp1} has 1 correct localization and N_{samp0} has 0 correct localizations. Then the $T(\mathbf{g}_+)$ histogram is made from the N_{samp2} $T(\mathbf{g}_+)$, plus $(1/2) \times$ the N_{samp1} $T(\mathbf{g}_+)$, plus $0 \times$ the N_{samp0} $T(\mathbf{g}_+)$. The composite histogram is normalized by

$$\frac{1}{N_{samp0} + N_{samp1} + N_{samp2}}.$$
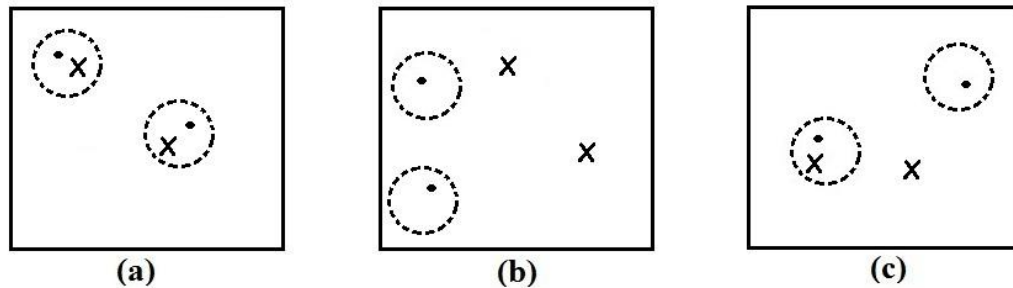
Figure 6.1 See text for explanation

What about the $T(\mathbf{g}_-)$ histogram? Let's say we had M_{samp} samples. Then all $T(\mathbf{g}_-)$ reports are included in the histogram and the histogram is normalized by M_{samp}.

Finally, the threshold T_0 is swept from $+\infty$ to $-\infty$ and the histograms integrated from T_0 to $+\infty$ to generate the AFROC curve as T_0 is swept. As before, numerical (trapezoidal) integration of the AFROC curve is used to get AAFROC.

6.3 Imaging details

In this Chapter, our imaging model for SPECT is still Eq.(5.1). And $\mathbf{H}$'s characteristics still hold. We conduct 2-D SPECT imaging trials as we did in Chapter 5.
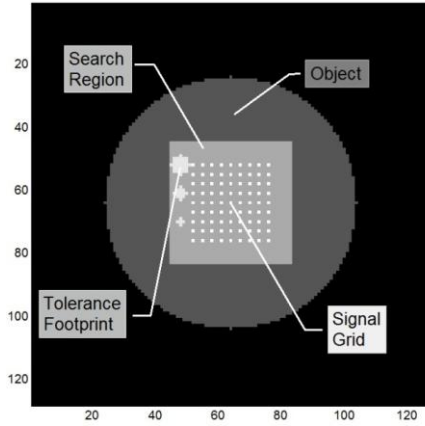
Figure 6.2 The SPECT Object (Higher Resolution)

We use a higher resolution object (128×128 vs. 64×64 for LROC) for AFROC experiments as shown in Figure 6.2. The object background is circular with radius equal to 40 pixels from the center pixel (64, 64). The entire object plane is the 128×128 black region as shown in Figure 6.2. The gray square is the search region $\mathbf{\Omega}$ (39×39 centered at (64,64)), which covers the area in which we search for signals. In other words, $\mathbf{\Omega}$ is the region over which we take a max and second max of the post-summation image. The one-pixel white spots are our signal grid ξ, which include all the true signal locations we may put signals on (from (52, 52), step equally by 3 pixels, totally 81 spots). We will try cases where the signal intensity is 16, 20, 25, 28 times that of the background. The numerical value of signal intensity in object space itself doesn't mean a lot, and only counts in sinogram has meaning to us. Note that ξ and $\mathbf{\Omega}$ need not be the same. The locations ξ are where true signals might appear in $\mathbf{f}_+$ and the search region $\mathbf{\Omega}$ contains

44

hypothesized locations. The tolerance footprints are also shown in Figure 6.2, from top to bottom, the radiuses are 3, 2 and 1.

Note that the ideal observer was for this AFROC case mathematically defined using continuous notation, where $\mathbf{r}$ is a 2-D location vector. But simulations are carried out on a discrete grid. It will be understood that for simulations, locations will take on discrete values. For example we will use $\mathbf{S}_{\mathbf{r}_1}$ to indicate a signal $\mathbf{S}$ in $\mathbf{f}$ located at $\mathbf{r}_1$. Here $\mathbf{r}_1$ is assumed to be discrete and $\mathbf{r}_1 \in \xi$.

In our simulation, our physical pixel size is 0.3125cm, and our bin size is also 0.3125cm. The distance from the object center (64,64, in pixel) to imaging plane is 35cm, We apply 129 equispaced angles over 2π around the object. The bin-number, that is the number of detectors in the gantry at any one angle, is 192, which is designed wide enough to capture all possible photons emitting from the object. In our experiment, we set the count level equal to 30,000, which is same as explained in detail in SPECT LROC experiment in Chapter 5. Note that the count level does not change as we go from a 64×64 object to a 128×128 object. In reality $\mathbf{f}$ is continuous and discretizing $\mathbf{f}$ is just needed for computer implementation. So even if $\mathbf{f}$ were continuous, we'd still have 30,000 counts on average.

As we stated in Chapter 3, AFROC tasks deal with the detection and localization of multiple signals, we have two signal in our object, $\mathbf{f}_+$. In our experiment, we lock the number of signals equaling to 2. In ξ, and the signals are separated by $2R$. In Ω, we search for 2 signals also separated by $2R$.

Our collimator model for AFROC experiment is the same as in Chapter 2. And we use the same collimator family as for LROC in Chapter 5. Figure 5.2 and Table 5.1 summarize the collimator family we will use here. Note that here we use higher resolution object for the than LROC experiment, but we meantime use smaller bins and pixels size which keep the object physical size the same and which will not affect the collimator values in Table 5.1.

6.4   AFROC experiment

To generate $\mathbf{g}_+$ images, we first generate $\mathbf{f}_+$ samples by adding two signals $\mathbf{S}_{\mathbf{r}_1}$ $\mathbf{S}_{\mathbf{r}_2}$ on ξ by probabilistic sampling with "Rejection Scheme". The rejection scheme basically randomly takes $\mathbf{S}_{\mathbf{r}_1}$ within ξ with uniform probability, then independently randomly takes $\mathbf{S}_{\mathbf{r}_2}$ with uniform probability. Calculate the distance between $\mathbf{S}_{\mathbf{r}_1}$ and $\mathbf{S}_{\mathbf{r}_2}$, and if it is $\le 2R$, we discard current $\mathbf{S}_{\mathbf{r}_2}$ and sample a new location for $\mathbf{S}_{\mathbf{r}_2}$ until the distance between $\mathbf{S}_{\mathbf{r}_1}$ and $\mathbf{S}_{\mathbf{r}_2}$ bigger than $2R$. We record $\mathbf{S}_{\mathbf{r}_1}$ and $\mathbf{S}_{\mathbf{r}_2}$'s locations as the vector $\mathbf{l}_{true}(\mathbf{f}_+^k)$, where k indexes sample number. With $\mathbf{f}_+^k$, we project it via (2.5) using MIPL-Sim to get $\mathbf{g}_+^k$. To generate $\mathbf{g}_-^k$, we simply use (2.5) and MIPL-Sim where $\mathbf{f}_-$ contains no signals. In our experiment, our N_{samp}^+ for $\mathbf{g}_+$ is 2,000 and N_{samp}^- for $\mathbf{g}_-$ is 1,000. We used more signal present samples because mislocalized observer location estimates are excluded or half excluded from the histogram due to the scoring method in section 6.3. Thus of the 2,000 signal-present responses, only a fraction make it to the $T(\mathbf{g}_+)$ histogram.

After accumulating N_{samp}^+ $\mathbf{g}_+$ and N_{samp}^- $\mathbf{g}_-$, we do the following: we apply the observer T in (6.5) on a given $\mathbf{g}^k$ as introduced in Chapter 3 to get $T(\mathbf{g}_+^k)$ and $T(\mathbf{g}_-^k)$ to obtain 2 observer responses, and 2 estimated locations for each image, indexed as $\mathbf{l}_{guess}(\mathbf{f}_+^k)$. For signal absent objects $\mathbf{f}_-^k$ with their associated $\mathbf{g}_-^k$, we do not need accumulate estimated locations $\mathbf{l}_{guess}(\mathbf{f}_-^k)$. While these estimated locations are indeed calculated as part of calculating $T(\mathbf{g}_-^k)$, we don't need to store them for scoring purposes. Compare $\mathbf{l}_{true}(\mathbf{f}_+^k)$ and $\mathbf{l}_{guess}(\mathbf{f}_+^k)$ and follow the same scoring method described in Sec 6.2 to see if the $\hat{\mathbf{r}}^k$ are within R of the $\hat{\mathbf{r}}^k$. We then accumulate histograms for $T(\mathbf{g}_+)$ and $T(\mathbf{g}_-)$.

Mathematically, our observer can be described in (3.7) and (3.8), and since the likelihood is separable, each factor in the likelihood is same as in (3.5). In (3.5), we used the notation $LR(\mathbf{g};\mathbf{s}_j)$. Now we'll use $LR(\mathbf{g};\mathbf{s}_{\mathbf{r}_j})$ where the lower case "$\mathbf{s}$" means a hypothesized signal and $\mathbf{s}_{\mathbf{r}_j}$ means it is located at $\mathbf{r}_j$, $j \in \Omega$. In this case

$$LR(\mathbf{g};\mathbf{s}_{\mathbf{r}_j}) = \prod_m e^{-[\mathbf{Hs}_{\mathbf{r}_j}]_m}(1+\frac{[\mathbf{Hs}_{\mathbf{r}_j}]_m}{[\mathbf{Hb}]_m})^{g_m} \qquad (6.6)$$

which is the same as (3.5) with a slight change in notation. Also in (6.1) we used expressions $LR(\mathbf{g};\mathbf{r}_1,\mathbf{r}_2)$ and $LR(\mathbf{g};\mathbf{r}_1)$ and it will be convenient to use interchangeably $LR(\mathbf{g};\mathbf{s}_{\mathbf{r}_1},\mathbf{s}_{\mathbf{r}_2})$ and $LR(\mathbf{g};\mathbf{s}_{\mathbf{r}_1})$ instead.

Pseudo-code of our software:

Precomputation for $\mathbf{Hs}_{\mathbf{r}_j}$, $j \in \Omega$ via MIPL-Sim for each collimator.

The software pipeline for a given collimator is then

For $k = 1$, N_{samp}^+

- Generate next $\mathbf{S}_{\mathbf{r}_1}, \mathbf{S}_{\mathbf{r}_2}$ pair for $\mathbf{f}_+^k$ and store in $\mathbf{l}_{true}(\mathbf{f}_+^k)$

- Generate $\mathbf{g}_+^k$ via (2.5) to project $\mathbf{f}_+^k$

End k

For $k = 1$, N_{samp}^-

- Generate $\mathbf{g}_-^k$ via (2.5) to project $\mathbf{f}_-^k$

End k

For $k = 1$, N_{samp}^-

- Generate $T(\mathbf{g}_-^k)$ via (6.5)

- Store the $T(\mathbf{g}_-^k)$ in histogram $T(\mathbf{g}_-)$.

End k

For $k = 1$, N_{samp}^+

- Generate $T(\mathbf{g}_+^k), \mathbf{l}_{guess}(\mathbf{f}_+^k)$ via (6.5)

- Compare $\mathbf{l}_{guess}(\mathbf{f}_+^k)$ to $\mathbf{l}_{true}(\mathbf{f}_+^k)$ to see if we have 0,1 or 2 correct localizations.

- Split the histogram into $N_{samp0}\, T(\mathbf{g}_+)$ for the 0-correct, $N_{samp1}\, T(\mathbf{g}_+)$ for the 1-correct and $N_{samp2}\, T(\mathbf{g}_+)$ for the 2-correct localizations.

- Weight the histograms and normalize them to get $T(\mathbf{g}_+)$ final histogram

End k

Store the histograms as described earlier and follow the integration procedures to
get AAFROC for that collimator.

Repeat for next collimator.

From coding point of view, some programming tricks inherited from Chapter 5 are applied
below:

a) For (3.5), $[\mathbf{Hs_{r_j}}]_m$, $[\mathbf{Hb}]_m$ and $e^{-[\mathbf{Hs_{r_j}}]_m}$ can be pre-computed, avoiding repeating
computation for each sample.

b) In scoring work, since the $T(\mathbf{g_+})$ and $T(\mathbf{g_-})$ are in a huge range, we take $\log(T(\mathbf{g_+}))$ and
$\log(T(\mathbf{g_-}))$ and then histogram them. Log transformation is monotonic, thus we won't lose any
information but get nice histograms shown in Figure 5.3. That is, if one integrates $T(\mathbf{g_-})$ and
$T(\mathbf{g_+})$ from T_0 to $+\infty$, the resulting integration is unchanged if we monotonically transform $T(\mathbf{g_-})$
and $T(\mathbf{g_+})$ before integration. Taking the log here is very different than taking the log of the
likelihood ratio.

6.5   Results

We calculated AAFROC vs. σ for 4 different signal intensities as shown in Figure 6.3. As
signal intensity rises, we expect AAFROC to rise and we observe that. The UHsens collimator is
the best collimator (significantly better than the GAP) for signal intensities $16\times$Background and
$20\times$Background so that the curves resemble the LROC results. However, at very high signal
intensities, AAFROC is maximized at the GAP. That is, the system performs best with a low
efficiency high resolution collimator if very high signal intensity is used.

It is not clear why this shift to high resolution/low efficiency occurs at high signal.
Apparently, the IO can deal with the noise in a low-efficiency image if the signal is strong
enough to differ from the noise background. For observer testing, one would prefer low intensity
signals since if one could do well with these, they'll be able to see the higher intensity signals
anyway.

6.6   Validity of the separability assumption

In Sec. 6.1, we mentioned two separability assumptions upon which the computationally efficient ideal observer in (6.5) holds. Here we discuss these assumptions.

The first assumption, that $p(\mathbf{r}_1, \mathbf{r}_2) \equiv p(\mathbf{r}_1) p(\mathbf{r}_2)$ is reasonable medically unless we have some extra information on the disease process. For example, for looking for liver metastases, there is no reason affects the location of the 2nd tumor. An exception is that the 2nd tumor be located some distance away from the first, a reasonable assumption given the finite size of real tumor, and given that separate tumors are reasonably separated by the $2R$ tolerance. This separation constraint makes the independence assumption technically invalid, but independence is still a good assumption.
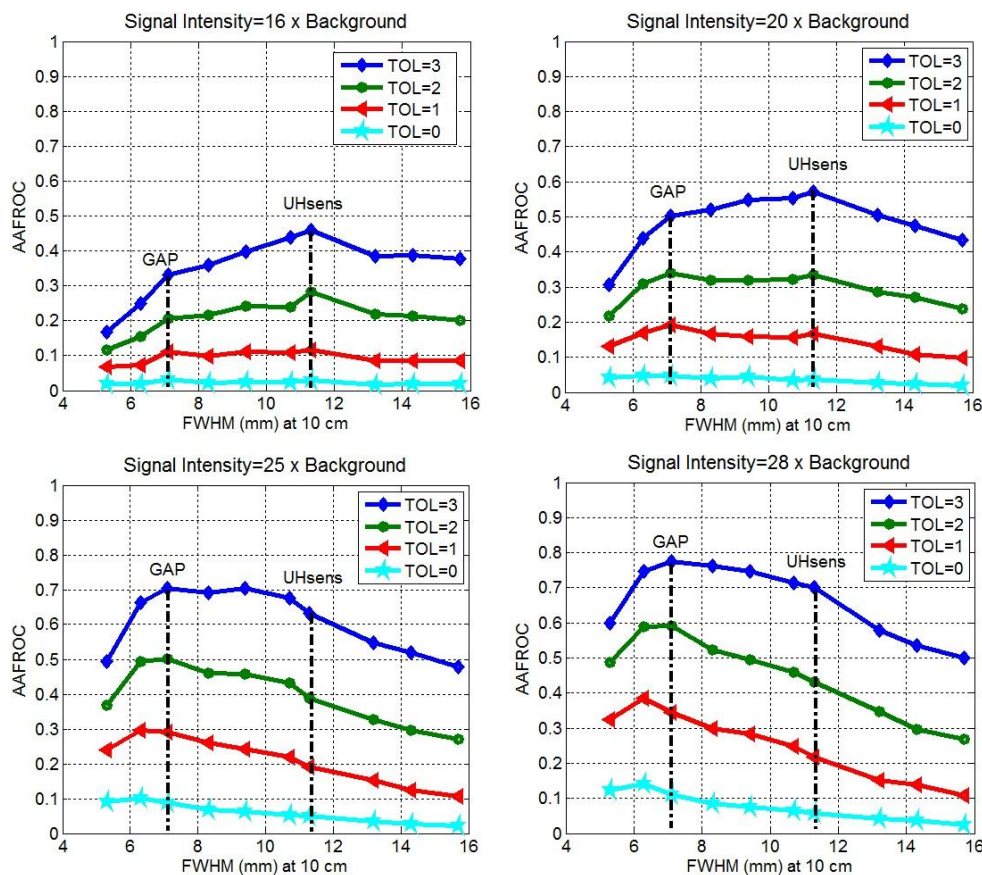

Figure 6.3 AAFROC vs. σ results for 4 different signal levels

What about the independence of the likelihood ratio $LR(\mathbf{g}; \mathbf{r}_1, \mathbf{r}_2)$? This is more difficult to verify. We did the following. For computational ease, we replaced the Poisson likelihood of (3.3) with a Gaussian likelihood, so that the signal-present likelihood becomes

$$p(\mathbf{g}\,|\,\mathbf{r}_1,\mathbf{r}_2) = (const.)e^{-\frac{(\mathbf{g}-\bar{\mathbf{g}})^T(\mathbf{g}-\bar{\mathbf{g}})}{2\sigma^2}} \tag{6.7}$$

where $\bar{\mathbf{g}}_+(\mathbf{r}) = \mathbf{Hb} + \mathbf{Hs}_{\mathbf{r}_1} + \mathbf{Hs}_{\mathbf{r}_2}$. The signal-absent likelihood becomes

$$p(\mathbf{g}\,|\,H_0) = e^{-\frac{(\mathbf{g}-\bar{\mathbf{g}})^T(\mathbf{g}-\bar{\mathbf{g}})}{2\sigma^2}} \qquad with \qquad \bar{\mathbf{g}} = \mathbf{Hb} \tag{6.8}$$

By setting $\sigma^2 = \mathbf{Hb}$, we obtain an independent but not identically distributed Gaussian whose variance = mean at all bins except where $\mathbf{Hs}_{\mathbf{r}}$ is non-zero. We take this as a reasonable approximation to the independent Poisson model. From (6.7) and (6.8), the likelihood ratio becomes

$$LR(\mathbf{g};\mathbf{r}_1,\mathbf{r}_2) = \frac{\exp\left[-\dfrac{(\mathbf{g}-\mathbf{Hb}-\mathbf{Hs}_{\mathbf{r}_1}-\mathbf{Hs}_{\mathbf{r}_2})^T(\mathbf{g}-\mathbf{Hb}-\mathbf{Hs}_{\mathbf{r}_1}-\mathbf{Hs}_{\mathbf{r}_2})}{2\mathbf{Hb}}\right]}{\exp\left[-\dfrac{(\mathbf{g}-\mathbf{Hb})^T(\mathbf{g}-\mathbf{Hb})}{2\mathbf{Hb}}\right]}$$

$$= \exp\left[\frac{2(\mathbf{g}-\mathbf{Hb})^T(\mathbf{Hs}_{\mathbf{r}_1}+\mathbf{Hs}_{\mathbf{r}_2}) - (\mathbf{Hs}_{\mathbf{r}_1}+\mathbf{Hs}_{\mathbf{r}_2})^T(\mathbf{Hs}_{\mathbf{r}_1}+\mathbf{Hs}_{\mathbf{r}_2})}{2\mathbf{Hb}}\right]$$

$$= \exp\left[\frac{2(\mathbf{g}-\mathbf{Hb})^T(\mathbf{Hs}_{\mathbf{r}_1}) - (\mathbf{Hs}_{\mathbf{r}_1})^T(\mathbf{Hs}_{\mathbf{r}_1})}{2\mathbf{Hb}}\right]$$

$$\times\exp\left[\frac{2(\mathbf{g}-\mathbf{Hb})^T(\mathbf{Hs}_{\mathbf{r}_2}) - (\mathbf{Hs}_{\mathbf{r}_2})^T(\mathbf{Hs}_{\mathbf{r}_2})}{2\mathbf{Hb}}\right]$$

$$\times\exp\left[-\frac{2(\mathbf{Hs}_{\mathbf{r}_1})^T(\mathbf{Hs}_{\mathbf{r}_2})}{2\mathbf{Hb}}\right]$$

$$= LR(\mathbf{g};\mathbf{r}_1)LR(\mathbf{g};\mathbf{r}_2)E(\mathbf{r}_1,\mathbf{r}_2)$$

where the "extra" term $E(\mathbf{r}_1,\mathbf{r}_2) = \exp\left[-\dfrac{2(\mathbf{Hs}_{\mathbf{r}_1})^T(\mathbf{Hs}_{\mathbf{r}_2})}{2\mathbf{Hb}}\right]$ should act as a constant (vary slowly

with $(\mathbf{r}_1,\mathbf{r}_2)$ with respect to $LR(\mathbf{g};\mathbf{r}_1)LR(\mathbf{g};\mathbf{r}_2)$) in order to maintain that $LR(\mathbf{g};\mathbf{r}_1,\mathbf{r}_2)$ is separable.

We conducted exhaustive numerical trials, given the object, $\mathbf{\Omega}$ and ξ described earlier, to see if this assumption held. For signal-present objects yielding $\mathbf{g}_+$ with signals at $\mathbf{S}_{\mathbf{r}_1}$ and $\mathbf{S}_{\mathbf{r}_2}$, the extra term varies very slowly and

$$LR(\mathbf{g}_+;\mathbf{r}_1,\mathbf{r}_2) \cong K \times LR(\mathbf{g}_+;\mathbf{r}_1)LR(\mathbf{g}_+;\mathbf{r}_2)$$

where K is approximately a constant, so separability holds.

For signal-absent images $\mathbf{g}_-$, the relative constancy of $E(\mathbf{r}_1,\mathbf{r}_2)$ was not as good. For relatively high tolerance (high R) and low efficiency collimators, the $E(\mathbf{r}_1,\mathbf{r}_2)$ term behaved well (was relatively constant) but as R shrank and the collimator became more efficient (longer tails on the depth psf) the $E(\mathbf{r}_1,\mathbf{r}_2)$ could vary by a factor of 2 or so across the range of $\mathbf{r}_1$ and $\mathbf{r}_2$ locations. For these cases, the observer in (6.5) was less than ideal. Clearly, this requires further work.

Chapter 7
Summary, Contributions and Future Work

In this chapter I summarize the results and also list the specific contributions I made. I comment on the directions someone might take to extend the work.

7.1 Summary

Detection and estimation performance is used to optimize medical imaging systems. The medical imaging system we studied was SPECT. In other words, an imaging system that lets someone search for and find lesions with better performance is better than that yields worse performance. Here performance was measured by the scalar ALROC and AAFROC produced by an ideal observer examining the sinogram. As discussed in (Barrett & Myers, 2003), good performance by an ideal observer on the sinogram should translate to good performance by a human observer examining a reconstructed image.

Specifically, the thing that was altered to change performance was the collimator. The depth-dependent nature of collimators and their efficiency was summarized and a collimator family of 10 collimators used. The best collimator for the LROC task was the ultra-high-sensitivity collimator, which yields blurry and smooth sinograms as compared to higher resolution collimators used in the clinic that yield noisier but higher resolution sinograms. For the AFROC task, the ultra-high-sensitivity collimator again yielded the best performance, but curiously, as signal contrast was upped to very high levels, lower efficiency higher resolution collimators were best.

7.2 Contributions

My work made use of the theoretical expressions for new ideal observers developed earlier in our group (Khurd & Gindi, 2005; Khurd et al., 2010; Liu et al., 2010) and used the MIPL-Sim software SPECT simulator also developed over many years in our group by students S.J. Lee, I.T.

Hsiao, W. Wang, Y. Huang, S. Kulkarni, Y. Xing and P. Khurd. I applied this theory and software tools to a problem in SPECT optimization.

For Chapter 6 I applied the ideal observer to SPECT for the 2-2 AFROC task. I wrote an extensive software package and addressed theory questions in formulating the AFROC results. This was the first application of the AFROC ideal observer to SPECT. The MATLAB code I wrote to carry this out was quite complex and contained many practical speedups to aid the long calculations, and interface with MIPL-Sim. In addition I formulated and carried out the separability tests described in Sec. 6.6. A remaining technical problem for the AFROC observer is to examine the separability issue of Sec. 6.6 more closely.

In Chapter 5, I applied the ideal observer to SPECT for the LROC task. This very goal was addressed earlier in our group in (Zhou & Gindi, 2009). But in (Zhou & Gindi, 2009), non-intuitive results were obtained. Later it was realized that this had to do with an unrealistically large search region. I redid the previous project, writing my own code, and carefully designed the object, search grid and signal grid to be more realistic. My results should that an optimal collimator (a peak in the ALROC vs. σ curve) could indeed be found, whereas for the earlier work, the ALROC curve rose monotonically with σ.

In Chapter 4 I conducted LROC studies using planar imaging. This was new and not done previously, but the main purpose of this work was to develop the infrastructure for my code that could be applied to the more complicated SPECT problems in Chapter 5 and 6. The planar results are not that useful in themselves.

In summary, my main contribution was Chapter 6, a secondary contribution in Chapter 5 and a minor contribution in Chapter 4. Naturally, my advisor suggested the problems and provided continuous advice, but the project was done by me alone. I contributed some mathematical insights in converting the ideal observer math to practical code as well as doing the coding.

7.3 Future directions

The collimators were modeled as if a photon hitting a septa is completely stopped by the collimator material. Under this assumption we get Eq.(2.3) and Eq.(2.4). However, in many clinical studies, the radionuclide will radiate photons at several energies. The higher energy

photons can penetrate the septal walls. The "septal penetration" effects are important in that the depth-dependent psf as seen in Figure 2.8 can change to include long low amplitude tails. Thus the **H** matrix is changed. This could change our results. Such problems have been studied elsewhere (Moore, Vries, Penney, Mueller, & Kijewski, 1998), but the studies did not use the same performance criteria as we did.

We did not model the important physical effect of scatter. Here, a photon can scatter from an atom in the body (Ogawa, Harata, Ichihara, Kubo, & Hashimoto, 1991) and enter the collimator as if it originated in the scatter site. This again changes the **H** matrix and hence the psf model we used could affect our results.

There are several clinical applications in SPECT to which our work could be applied. These applications are in oncology where the physician surveys the body looking for localized hot spots in radionuclide uptake indicating tumors or metastases.

Finally, I note that the main results of the work, the ALROC and AAFROC vs. σ plots of Figure 5.5 and Figure 6.3 did not include error bars. However, I am confident that with the sample sizes used ($N_{samp} \sim 10^3$) the errors are well below 1%. This conclusion is based on work by (Zhou & Gindi, 2009) and (Kulkarni, Khurd, Hsiao, Zhou, & Gindi, 2007) who used bootstrap techniques (Zoubir & Boashash, 1998) in situations similar enough to mine that it seems that the sample error will be negligible. Nevertheless, this would have to be confirmed.

Reference

Barrett, H. H., & Myers, K. J. (2003). *Foundations of Image Science*. New York: Wiley Interscience.

Barrett, H. H., & Swindell, W. (1981). *Radiological Imaging: Theory of Image Formation, Detection and Processing* (Vol. **I**). New York: Academic Press.

Clarkson, E. (2007). Estimation Receiver Operating Characteristic Curve and Ideal Observers for Combined Detection/Estimation Tasks. *Journal of the Optical Society of America A, 24*, B91-B98.

Kay, S. (1998). *Fundamentals of Statistical Signal Processing: Detection Theory* (Vol. **2**).

Khurd, P. (2005). *On Reconstruction Methods and Image Quality in Emission Tomography. Ph.D.* , Department of Electrical and Computer Engineering, Stony Brook University.

Khurd, P., & Gindi, G. (2005). Decision Strategies that Maximize the Area Under the LROC Curve. *IEEE Trans. Med. Imaging, 24*(12), 1626-1636.

Khurd, P., Liu, B., & Gindi, G. (2010). Ideal AFROC and FROC Observers. *IEEE Transactions on Medical Imaging, 29*(2), 375-386.

Kulkarni, S., Khurd, P., Hsiao, I.-T., Zhou, L., & Gindi, G. (2007). A Channelized Hotelling Observer Study of Lesion Detection in SPECT MAP Reconstruction Using Anatomical Priors. *Phys. Med. Biol., 52*(12), 3601-3617.

Lamberts, S. W. J., Chayvialle, J. A., & Krenning, E. P. (1992). The Visualization of Gastroenteropancreatic Neuroendocrine Tumors. *Metabolism, Suppl, 41*(2), 111-115.

Liu, B., Khurd, P., & Gindi, G. (2010). Rapid Performance Evaluation for Ideal FROC and AFROC Observers. *Proc. of SPIE, 7627*, 0V1-10.

Metz, C. (1978). Basic Principles of ROC Analysis. *Seminars in Nuclear Medicine, 8*, 293-298.

Moore, S. C., Vries, D. J., Penney, B. C., Mueller, S. P., & Kijewski, M. F. (1998). Design of A Collimator for Imaging In-111. In M. Ljungberg, S. Strand & M. A. King (Eds.), *Monte Carlo Calculations in Nuclear Medicine Applications in Diagnostic Imaging* (pp. 183-193). UK: Institute of Physics Publishing

Myers, K. J. R., J.P.; Barrett, H.H.; Wagner, R.F. (1990). Aperture Optimization for Emission Imaging: Effect of A Spatially Varying Background. *Journal of the Optical Society of America A* **7**, 1279-1293.

Ogawa, K., Harata, Y., Ichihara, T., Kubo, A., & Hashimoto, S. (1991). A Practical Method for Position-Dependent Compton-Scatter Correction in Single Photon Emission CT. *IEEE Trans. Med. Imaging, 10*(3), 408-412.

Parker, & Anthony, J. (2011). Joint Program in Nuclear Medicine, from http://www.med.harvard.edu/JPNM/CH/Sept2303/BoneSPECT.jpg

Swensson, R. (1996). Unified Measurement of Observer Performance in Detecting and Localizing Target Objects on Images. *Medical Physics, 23*(10), 1709-1725.

Wang, W. (1997). *Noise Analysis of Bayesian Reconstruction Algorithms in Emission Tomography. Ph.D.*, Department of Electrical and Computer Engineering, Stony Brook University.

Wernick, M. N., & Aarsvold, J. (2004). *Emission Tomography: the Fundamentals of PET and SPECT*: Elsevier Academic Press.

Xing, Y. (2003). *Rapid Calculation of Detectability for Maximum a Posteriori Reconstructions in SPECT. Ph.D.*, Department of Electrical and Computer Engineering, Stony Brook University.

Yale University School of Medicine. (2004). Cardiac Anatomy as Seen in SPECT Nuclear Imaging, from http://www.yale.edu/imaging/techniques/spect_anatomy/index.html

Zhou, L., & Gindi, G. (2009). Collimator Optimization in SPECT Based on a Joint Detection and Localization Task. *Physics in Medicine and Biology, 54*, 4423-4437.

Zhou, L., Khurd, P., Kulkarni, S., Rangarajan, A., & G, G. (2008). Aperture Optimization in Emission Imaging Using Ideal Observers for Joint Detection and Localization. *Physics in Medicine and Biology, 53*, 2019-2034.

Zhou, L., Kulkarni, S., Liu, B., & Gindi, G. (2009). Strategies to Jointly Optimize SPECT Collimator and ReconstructionParameters for a Detection Task. *Symposium on Biomedical Imaging Proc. IEEE Itnl.*, 394-397.

Zoubir, A. M., & Boashash, B. (1998). The Bootstrap and its Appicaltion in Signal Processing. *IEEE Signal Proc. Mag., 15*, 56-76.